

AD-A153 156

ANALYSIS AND MODELING FOR THERMAL FOCAL PLANE ARRAYS

172

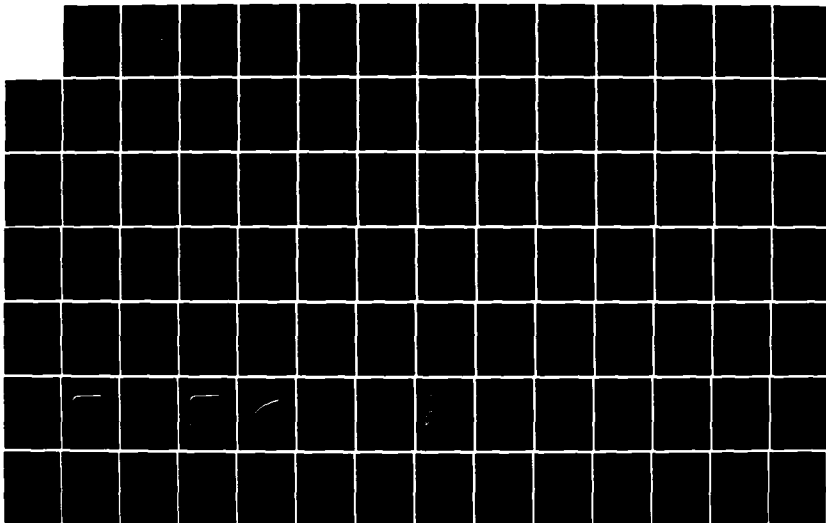
(U) NICHOLS RESEARCH CORP ANN ARBOR MI T W TIER ET AL.

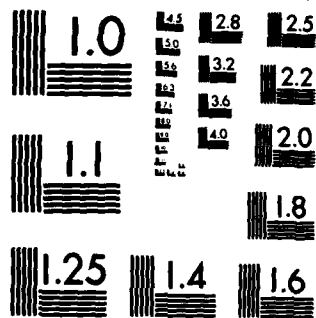
10 JUL 84 NRCAR-TR-84-001 DAK70-83-C-0026

UNCLASSIFIED

F/G 14/2

NL





MICROCOPY RESOLUTION TEST CHART
NATIONAL BUREAU OF STANDARDS-1963-A

②

NRCAA-TR-84-001

ANALYSIS AND MODELING FOR THERMAL FOCAL PLANE ARRAYS

SCIENTIFIC AND TECHNICAL REPORT
FINAL TECHNICAL REPORT

10 JULY 1984

CDRL A004

CONTRACT DAAK70-83-C-0026

PREPARED FOR:

NIGHT VISION & ELECTRO-OPTICS LABORATORY
DELNV-IRTD/ANTHONY T. DE PERSIA
FORT BELVOIR, VIRGINIA 22060

DTIC
ELECTE
APR 26 1985
S E

"The views, opinions and/or findings contained in this report are those of the author and should not be construed as an official Department of the Army position, policy, or decision, unless so designated by other documentation."

This document has been approved
for public release and sale; its
distribution is unlimited.

Nichols
Research
Corporation

2002 HOGBACK ROAD, SUITE 19
ANN ARBOR, MICHIGAN 48104

DTIC FILE COPY

85 04 01 112

AD-A153 156

**Nichols
Research
Corporation**

2002 HOGBACK ROAD, SUITE 19
ANN ARBOR, MICHIGAN 48104

**ANALYSIS AND MODELING FOR THERMAL FOCAL
PLANE ARRAYS**

**SCIENTIFIC & TECHNICAL REPORT
FINAL TECHNICAL REPORT**

10 JULY 1984

CDRL A004

PREPARED BY:

THOMAS W. TUER
BRUCE W. BALL
J. RICHARD FREELING
JOHN W. LENNINGTON
GEORGE H. LINDQUIST
JOSEPH MUDAR

PREPARED FOR:

NIGHT VISION AND ELECTRO-OPTICS LABORATORY
DELVN-IRTD/ANTHONY T. DePERSIA
FORT BELVOIR, VIRGINIA 22060

Accession For	
NTIS GRA&I	<input checked="" type="checkbox"/>
DTIC TAB	<input type="checkbox"/>
Unannounced	<input type="checkbox"/>
Justification	
By	
Distribution/	
Availability Codes	
Dist	Avail and/or Special
A-1	



CONTRACT DAAK70-83-C-0026

This document has been approved
for public release and its
distribution is unlimited.

REPORT DOCUMENTATION PAGE		READ INSTRUCTIONS BEFORE COMPLETING FORM
1. REPORT NUMBER	2. GOVT ACCESSION NO.	3. RECIPIENT'S CATALOG NUMBER
4. TITLE (and Subtitle) Analysis and Modeling for Thermal Focal Plane Arrays		5. TYPE OF REPORT & PERIOD COVERED Final Report
7. AUTHOR(s) Thomas W. Tuer, Bruce W. Ball, J. Richard Freeling, John W. Lennington, George H. Lindquist, and Joseph Mudar		6. PERFORMING ORG. REPORT NUMBER NRCAA-TR-84-001
9. PERFORMING ORGANIZATION NAME AND ADDRESS Nichols Research Corporation 2002 Hogback Road, Suite 19 Ann Arbor, MI 48104		8. CONTRACT OR GRANT NUMBER(s) DAAK70-83-C-0026
11. CONTROLLING OFFICE NAME AND ADDRESS		10. PROGRAM ELEMENT, PROJECT, TASK AREA & WORK UNIT NUMBERS
14. MONITORING AGENCY NAME & ADDRESS (if different from Controlling Office)		12. REPORT DATE 10 July 1984
		13. NUMBER OF PAGES 106
		15. SECURITY CLASS. (of this report) Unclassified
16. DISTRIBUTION STATEMENT (of this Report) Unlimited		15a. DECLASSIFICATION/DOWNGRADING SCHEDULE None
17. DISTRIBUTION STATEMENT (of the abstract entered in Block 20, if different from Report)		
18. SUPPLEMENTARY NOTES		
19. KEY WORDS (Continue on reverse side if necessary and identify by block number) Infrared; Thermal Detectors; Pyroelectric Detectors; Focal Plane Arrays; Computer Simulation; Literature Survey.		
20. ABSTRACT (Continue on reverse side if necessary and identify by block number) The development of a first principles computer simulation of a generic pyroelectric thermal detector is described. Formulation of the pertinent equations (based on a thorough literature survey) is presented. This simulation incorporates a finite difference treatment of the transient three-dimensional thermal response of composite focal plane arrays, with treatments of the signal generation, readout and processing including all pertinent noise sources. A number of simplified problems having analytical solutions were treated to validate various portions of the simulation to within a few percent. Performance estimates were made for conceptual several configurations and materials. - <i>see cont. for summary include</i>		

FOREWORD

The authors would like to recognize the efficient direction of the contract by Mr. Anthony T. DePersia of the U.S. Army Night Vision and Electro-Optics Laboratory; the careful preparation of the manuscript by Barbara Pearlman and Kathleen Buchmann; reliable computer coding by Stephen Buchbinder, and the helpful discussions with Texas Instruments, and Dr. Butler of Honeywell Electro-Optics Division regarding their respective systems.

The views, opinions and/or findings contained in this report are those of the authors and should not be construed as an official Department of the Army position, policy, or decision, unless so designated by other documentation.

TABLE OF CONTENTS

	PAGE
SECTION 1. INTRODUCTION	1
SECTION 2. SUMMARY.	2
SECTION 3. LITERATURE SURVEY	4
SECTION 4. FORMULATION.	5
4.1 Thermal Formulation.	5
4.2 Electrical Model.	11
General Temperature Change to Voltage Conversion	11
Electrical Modeling	14
Focal Plane Output Voltages	16
Generalized Modeling	22
Formulation of Noise Components, NEP and D* for Pyroelectric Detector/CCD Readout	32
SECTION 5. CODE DESCRIPTION	42
5.1 Preprocessor	42
5.2 Processor	46
5.3 Postprocessor	46
SECTION 6. CODE VALIDATION	48
Check Cases A Through D	48
Check Case A	48
Check Case B	49
Check Case C	52
Check Case D	52
Check Cases E Through J	55
Check Case E	57
Run E-1	58
Run E-2	58
Run E-3	58
Run E-4	58
Run E-5	61
Run E-6	61

Table of Contents (Continued)

	PAGE
Check Case F	61
Run F-1	64
Run F-2	65
Run F-3	65
Run F-4	65
Check Case G	65
Run G-1	67
Check Case H	67
Check Case I	67
Run I-1	68
Run I-2	69
Run I-3	69
Run I-4	69
Run I-5	70
Run I-6	70
Check Case J	70
Run J-1	71
SECTION 7. EVALUATION OF TYPICAL THERMAL FOCAL PLANE ARRAYS	72
LiTaO ₃ , PVF ₂ and DTGFB Detector Arrays	72
BaTiO ₃ Detector Arrays	73
Responsivity and Crosstalk	73
Chopping Frequency	75
Array Materials and Dimensions	75
Code Variables	76
Approximate Line Source Widths	76
Irradiance Levels	76
HEOD's Models	76
SECTION 8. RESULTS	78
SECTION 9. CONCLUSIONS	79

Table of Contents (Concluded)

	PAGE
SECTION 10. RECOMMENDATIONS	80
REFERENCES	82
APPENDIX A. THERMAL AND ELECTRIC PROPERTIES OF PYROELECTRIC MATERIALS AT AMBIENT TEMPERATURE	83
APPENDIX B. THERMAL PROPERTIES OF PEDESTAL, ELECTRODE AND SUBSTRATE MATERIALS	84
APPENDIX C.	85

LIST OF FIGURES

FIGURE NO.	TITLE	PAGE
1	Thermal Node Structure, Coordinate System and Notation	3
2	Representative Indirect Charge Injection	15
3	CCD Data Flow	15
4	Circuit of CCD Charge Injection Scheme	17
5	Linear Model of TFPA Devices	24
6	System Noise Equivalent Model	32
7	Temperature History of an Insulated, Thermally Lumped, Detector Under Constant Irradiance, Check Case A	50
8	Comparison of Thermal Focal Plane Array Model With Exact Theory (Case B)	51
9	Comparison of Thermal Focal Plane Array Model With Exact Theory (Case C)	54
10	Comparison of Thermal Focal Plane Array Model With Exact Theory (Case D)	56
11	Code Results for Check Case E, Showing the Beginning of the Formation of the Theoretical Distribution, Run E-1	59
12	Comparison of Equilibrium Temperatures for Half-Irradiated Slab from Check Case E, Run E-4 and From Theory	60
13	Comparison of Equilibrium Temperatures for Half-Irradiated Slab from Check Case E, Run E-5 and From Theory	62
14	Comparison of Temperatures for Half-Irradiated Slab Losing Heat by Convection, Check Case E, Run E-6 and From Theory for the Equilibrium Case	63
15	Comparison of Equilibrium Temperatures for Detector Slab Irradiated Sinusoidally Along Its Length from Check Case F, Run F-3 and From Theory	66

List of Figures (Concluded)

FIGURE NO.	TITLE	PAGE
16	Detector Array Modeled in Test Case H	68
17	Comparison of Thermal Responsivity Versus Chopping Frequency Plots from HEOD's Nodal Analysis Code and From NRC's TFPA Code	77
18	Focal Plane Coordinates for (M,N) th Detector	86

LIST OF TABLES

TABLE NO.	TITLE	PAGE
1	Check Cases A Through J	53
2	NRC Simulation Generated Thermal Responsivities and Crosstalks for Typical Thermal Focal Plane Arrays	74
3	Comparison of Thermal Crosstalk Results for HEOD and Present Models	77
4	Percent Error in Code Versus Theory Prediction at ΔT Versus Time	78

SECTION 1. INTRODUCTION

This report documents the research and development work on a computer simulation of a pyroelectric thermal focal plane array by Nichols Research Corporation. This model is completely operational and described in software documents [1,2]. The present description is intended primarily for individuals who would like details of the model's formulation, range of applicability, assumptions, approximations and results. These topics are summarized in Section 2.

Section 3 of this document covers the results of the literature survey. Main outputs of the survey are an annotated bibliography which is published in a separate volume [3], and tables of pyroelectric system parameters given in Appendices A and B.

Section 4 presents the details of the formulation of thermal and electrical parts of the model. Included in the thermal formulation are the conductive, radiative and convective exchange within and between the detectors. The electrical formulation includes relating detector voltages to their temperature changes; the various transfer functions involved in signal readout, amplification and processing; and the formulation of system performance parameters.

The numerical procedures that were used in the computer code to evaluate its outputs are described in Section 5. Procedures for the preprocessor, processor and postprocessor are covered in Sections 5.1, 5.2 and 5.3 respectively.

A wide variety of validations of the code were run against exact analytical solutions to theoretical situations that test various parts of the code (see Section 6). Included in these tests are different boundary conditions and configurations to verify the conductive, radiative and convective procedures used. In Section 7, we evaluated the responsivity and crosstalk parameters of typical systems irradiated by a temporally chopped line source, and compared the results to similar analyses on a typical state-of-the-art system. Finally, the conclusions and recommendations of the study are discussed in Sections 8 and 9, respectively.

SECTION 2. SUMMARY

The development of the computer simulation for pyroelectric thermal focal plane arrays was based on a thorough survey of the available literature and on discussions with several system developers. The model can handle several general system configurations with arbitrary thermal and electrical properties. It treats the transient three-dimensional thermal response of the detector material and the associated electrodes, insulation and interconnectors, as they are influenced by arbitrarily specified, chopped thermal radiation and other environmental heat transfer mechanisms (see Figure 1).

A finite difference numerical solution was developed to consider general conductive, radiative and convective heat transfer within and between pyroelectric detector elements. The user can specify nonreticulated or fully reticulated focal planes. The fully reticulated gaps can be backfilled with arbitrary insulation or gas, or completely evacuated. Arbitrary focal plane configurations can be treated with arbitrary internal thermal node resolution within practical computer run time and storage limitations. The signal production, readout, and processing mechanisms and their associated noise sources are fully modeled with currently accepted theoretical expressions.

Various system performance parameters such as the modulation transfer function (MTF), detectivity (D^*), responsivity, and noise equivalent power are automatically evaluated for the simulated sensor. The frequency response of several sensors modeled by Honeywell Electro-Optics Division (HEOD) are in general agreement, but about a factor of two below those predicted by the present model.

A variety of validations to the thermal model were completed using different exact solutions such as one-dimensional heat transfer with a number of boundary conditions. These computer runs generally checked to within one percent of exact solutions for pertinent situations. Comparisons with modeled crosstalk results published by HEOD show agreement to within about 5 percent.

The code was designed to be user-friendly and highly modular to facilitate modifications and upgrades. It is thoroughly documented both internally (by comment cards and the use of meaningful names for code parameters, functions, and subroutines), and externally (by a User's Manual [1] and a Software Maintenance Manual [2]).

The major development efforts on the TFP model since the Interim Report [4] were on the radiative and convective heat transfer between detector elements, the relationship between detector temperature voltage, and a postprocessor that treats all readout and signal processing operations and their related noise contributions. It was found that radiative and convective transfer generally has a negligible effect on MTF and crosstalk.

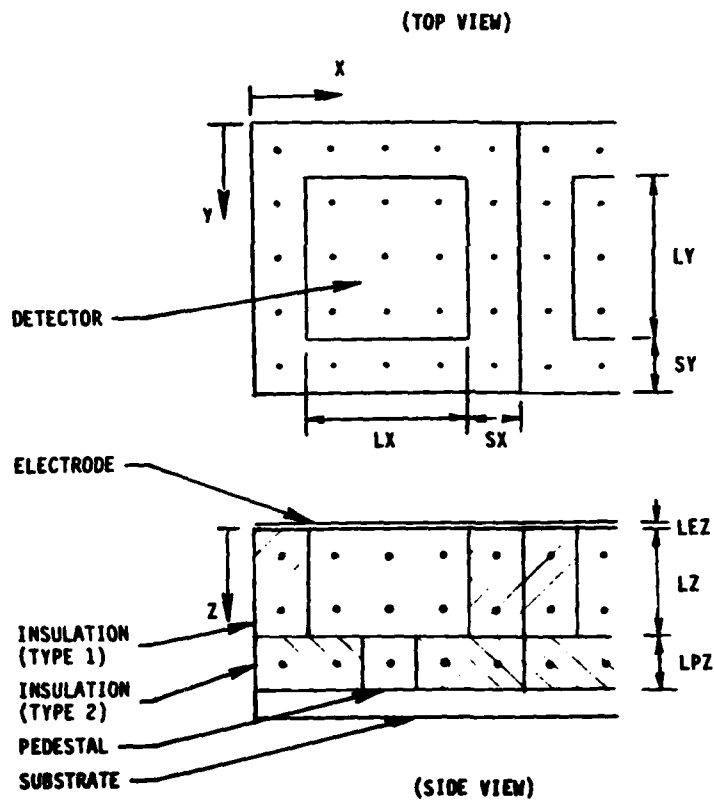


FIGURE 1. THERMAL NODE STRUCTURE, COORDINATE SYSTEM AND NOTATION.

SECTION 3. LITERATURE SURVEY

The objective of this task was to gather all available documentation on pyroelectric detectors with special concern toward material properties, and treatments of signal and noise processes within the detector. Our approach was to conduct computerized searches at the "DIALOG" information storage and retrieval system and the ERIM/IRIA Center document library. Other major sources were the Night Vision and Electro-Optics Laboratory (NVEOL), and references from collected documents. Of the original collection of 221 documents that were referenced in our Interim Report [4], a group of 150 of the most pertinent was annotated and published in a separate volume [3]. In addition, several of the most promising documents of that group were reviewed in detail to determine the most appropriate thermal and electrical modeling procedures. These are referenced as they are discussed later in this report (especially Section 4).

All of the original list of documents were also reviewed for information on material properties of pyroelectric materials. A table of pyroelectric parameters (pyroelectric constant, dielectric constant, and dielectric loss tangent) and thermal properties (thermal conductivity, specific heat per unit mass, mass density per unit volume, and thermal diffusivity) are given for 38 different materials (see Appendix A). (Not all the properties were available for all the materials.) The source of these properties are fully referenced. A complementary table of thermal properties is given (see Appendix B) for 16 different typical insulation and separation materials used in a thermal focal plane array. These sources are also fully referenced.

SECTION 4. FORMULATION

The objective of this section is to fully document NRC's formulation of the thermal and electrical equations that are amenable to computer solution. The approximations invoked are fully described and the limits of applicability of the solution indicated. Most of this development is not new but rather a compilation of existing treatments which will be fully referenced. Subsections 4.1 and 4.2 cover the thermal and electrical formulations, respectively.

4.1 THERMAL FORMULATION

The volumetric averaged temperatures of the individual detector elements of the array are required as a function of time in order to predict the detector output voltage. The model must be capable of treating rather general geometrical configurations (see Figure 1) for the elements with arbitrary thermal properties under arbitrary thermal boundary conditions. We have retained the three-dimensional capability in order to handle general detector arrays under any irradiance patterns.

The usual three-dimensional heat conduction equation for an isotropic material with constant thermal properties is:

$$\frac{\partial T}{\partial t} = \kappa \left(\frac{\partial^2 T}{\partial x^2} + \frac{\partial^2 T}{\partial y^2} + \frac{\partial^2 T}{\partial z^2} \right) \quad (1)$$

where T is the temperature of the material as a function of time t and the three orthogonal spatial coordinates (x,y,z) , and κ is the thermal diffusivity of the material. The boundary conditions we employ are (1) a uniform initial temperature distribution:

$$T(x,y,z,0) = T_0 \quad (2)$$

and (2) the radiative, convective, and conductive heating or cooling specification at the exterior surfaces.

This second set of boundary conditions depends on the details of the system configuration being modeled. The irradiated surface of the detector ($z=0$) has a net radiative gain per unit area of:

$$\dot{q}_{\text{rad}} = \alpha E(x,y,t) + \epsilon \sigma [T_b^4 - T(x,y,0,t)^4] \quad (3)$$

where E is the spatial irradiance difference from a blackbody environment at a uniform background temperature T_b , α and ϵ are the absorptance and emittance of the irradiated surface, and σ is the Stefan-Boltzmann constant.

The convective heat transfer is generally given by:

$$\dot{q}_{\text{conv}} = h[T_g - T(x,y,0,t)] \quad (4)$$

where h is a correlation constant and the ambient gas is taken to have a constant uniform temperature T_g . To evaluate the constant h , we used published correlation results for natural convection to surfaces in air [5]. These correlations are given for different orientations and thermal conditions (such as vertical and horizontal plates hotter or cooler than the ambient gas). We have used the correlation for vertical plates since the orientation of the surfaces is unknown, but vertical orientation is most likely.

$$hL/k_f = 0.555 (\text{GrPr})^{1/3} \quad (5)$$

where L is the characteristic length (taken to be the length of the detector), k_f is the thermal conductivity of the gas film over the surface, Gr is the Grashoff number and Pr is the Prandtl number. Typical room temperature values of k_f and Pr were taken from Reference 5. The Grashoff number is given by:

$$\text{Gr} = \beta g L^3 \Delta T / \nu^2 \quad (6)$$

where $\beta g/v^2$ is given by Kreith [5]. Using a nominal characteristic length ($L = 10^{-4}$ m), we find:

$$h = 1.71 \Delta T^{1/3} \text{ J}\cdot\text{s}^{-1}\cdot\text{m}^{-2}\cdot\text{K}^{-1} \quad (7)$$

so

$$\dot{q}_{\text{env}} = 1.71 [T_g - T(x,y,0,t)]^{4/3} \quad (8)$$

where the units of \dot{q} are $\text{J}^{-1}\cdot\text{m}^{-2}$, when T is in K.

The boundary condition at the other surfaces of the detector depend on the details of the array configuration. For example, one option of the code allows for insulation material between adjacent detectors in the array. In this case, we neglect radiative and convective heat transfer from these surfaces, but consider instead the conduction of heat through the insulation. The boundary conditions simply match the energy flow from one surface to the energy flow to the adjacent surface. That is, the heat leaving the side of the detector must equal the heat entering the insulator at the same point. Other boundary conditions are specified similarly.

In order to solve the heat conduction equation (see Equation 1) numerically on the computer, we expand it in finite difference form [6]:

$$\begin{aligned} C(i,j,k) [T(i,j,k,t + \Delta t) - T(i,j,k,t)] = \\ = \sum_{i'=1}^{n'_i} \sum_{j'=1}^{n'_j} \sum_{k'=1}^{n'_k} K(i,j,k; i',j',k') [T(i',j',k',t) - T(i,j,k,t)] \Delta t \end{aligned} \quad (9)$$

where C is the heat capacity of the node and the K 's are the thermal conductances for the paths to the adjacent nodes (indicated by the primes). The left side represents the energy increase of the node in terms of its temperature

rise during the time period, and the right represents the heat conducted into the node based on temperatures of the previous time t . As was discussed earlier [4], we selected the explicit treatment for programming expediency, but would recommend investigation of the implicit procedures such as Crank-Nicholson and others, that assure convergence.

In this equation, the temperature of the node under consideration at the previous calculational time $T(i,j,k,t)$, has a coefficient $(1 - t/\tau)$, where the characteristic time is:

$$\tau \equiv C(i,j,k) / \left[\sum_{i'=1}^{n_1} \sum_{j'=1}^{n_j} \sum_{k'=1}^{n_k} K(i,j,k;i',j',k') \right] \quad (10)$$

This characteristic time provides the criterion for absolute stability. It can be seen by inspection that when the time step Δt is greater than this parameter, the dependency on the temperature of the node at the previous calculational time becomes negative, implying instability. The preprocessor of the simulation effectively finds the largest allowable value of $\tau(i,j,k)$ for all directions guiding the user to select a proper value of the calculational time step Δt to assure calculational stability.

The top surface boundary condition involves the optical properties ($\alpha\epsilon$) of the absorbing material. We are assuming here that the focused radiation (E) would be filtered so that the absorptance (α) should be evaluated for the bandpass of the instrument and for the directions of the incident radiation. The emittance (ϵ) should be hemispherical and integrated over all wavelengths. We have assumed in our calculations to date that α and ϵ are equal to a nominal value given in Appendix A, although arbitrary values can also be assigned to each. At present, we can select the effective background temperature, T_b , independent of the ambient gas temperature T_g to accommodate more general background-atmospheric-operating conditions. The chopper irradiance can be specified in a general manner to account for the arbitrary conditions.

The boundary conditions on the sides of the detectors were also made as general as possible. The user can specify a solid material between the detector elements having any real value of thermal conductivity (k) desired independent of the materials below the detectors. Thus, any theoretical (e.g., a perfect insulation with $k=0$), or realizable conductivity such as for any typical insulators (see Appendix B), can be handled. Non-reticulated detectors or fully reticulated detectors can also be treated by proper selection of material properties. (Reticulated detectors are separated by a gap to reduce heat transfer between adjacent detector elements.)

Stagnant gas, such as may be found in the spaces between detectors, and between detectors and the substrate material can also be modeled with a different value of conductivity and heat capacity. It is difficult to model gas in this way, however, since extremely small time steps are required for stability (see Equation 10).

Convective and/or radiative boundary conditions can be specified for the sides and bottoms of the detectors. The convective heat transfer coefficient for these surfaces has default values based on the same correlations as the ones used for the top surface. This can be set to any value (including zero) for modeling evacuated or partially evacuated systems.

The radiative transfer between detectors, and between detectors and the substrate is treated assuming that only the two directly opposing nodes are directly controlling the heat transfer. That is, we consider parallel rectangular surfaces of equal size (representing the two opposing nodes) separated by a distance, D. All other surfaces of the radiative enclosure are assumed to absorb just as much heat as they emit (so-called "refractory surfaces"). For this situation, the net heat transfer from Surface 1 to Surface 2 is [7]:

$$\dot{Q}_{12} = AF'_{12}\sigma (T_1^4 - T_2^4) \quad (11)$$

where the upper case Q implies the total heat flux over A, the area of either surface. The radiation factor F'_{12} is given for diffuse, gray surfaces as:

$$F'_{12} = (1/\epsilon_1 + 1/\epsilon_2 + 1/F_{12})^{-1} \quad (12)$$

The geometrical radiation exchange factor F_{12} is given by Kreith for equal parallel rectangles with width W and length L , and separated by a distance D [5]:

$$F_{12} = \frac{2}{\pi uv} \ln \left\{ \left[\frac{(1+u^2)(1+v^2)}{1+u^2+v^2} \right]^{\frac{1}{2}} + v(1+u^2)^{\frac{1}{2}} \tan^{-1} \left[\frac{v}{(1+u^2)^{\frac{1}{2}}} \right] \right. \\ \left. + u(1+v^2)^{\frac{1}{2}} \tan^{-1} \left[\frac{u}{(1+v^2)^{\frac{1}{2}}} \right] - u \tan^{-1}(u) - v \tan^{-1}(v) \right\} \quad (13)$$

where $u = D/L$ and $v = D/W$. The radiative exchange between the bottom of the detector and the substrate is evaluated the same way with the area in Equation 11 taken to be the bottom surface area of the detector node. We have found, however, that for the low temperature and small temperature differences encountered in this problem that the radiative exchange is negligible compared to convection or conduction.

The conductive heat transfer boundary condition for the bottom of the detector considers a pedestal exchanging heat with the substrate. This pedestal can be surrounded by a second insulation material at the user's option. Thus, the thermal properties (conductivity and heat capacity) of the pedestal and two different insulation materials can be specified separately.

It should be noted that our lower boundary condition assumes a constant temperature (i.e., thermally massive) substrate. Texas Instruments concurs with these approximations for their system. On the other hand, HEOD's thermal model [8] considers a thermal conduction path between the detectors through the substrate.

4.2 ELECTRICAL MODEL

The thermal model provides a means whereby the temperature of the array, as a function of position and time, can be determined as a result of the input irradiance pattern upon it. These temperature changes are translated into voltages within the array, and passed through a readout mechanism to be ultimately analyzed or displayed. The electrical portion of the model must describe the temperature change to voltage conversion process, and the circuitry used to extract voltages from the array.

In addition, electronic noise, generated in the array elements, must also be modeled. These noises are amplified together with the noises generated within the readout structure to produce variations in the array output which are uncharacteristic of the input scene.

Once the electrical characteristics and the noises are modeled, the performance of the array system can be modeled in terms of parameters traditionally used to describe the performance of real devices, such as MTF, noise equivalent power (NEP), responsivity, and specific detectivity (D^*). The ultimate usefulness of this code comes from its ability to model both the thermal and electrical characteristics of thermal arrays. In this way, the expected performance of arrays can be assessed in terms of their characteristics without the requirement to actually build and test an example.

General Temperature Change to Voltage Conversion

The transduction of temperature change to voltage in the subject arrays occurs through the pyroelectric effect. The spatial temperature variations in the array are due to spatial variations in the radiative heat load. For a given 1/2 chopping cycle time Δz , a given detector element (M,N) will experience an effective temperature change ΔT . A surface electric charge is generated on the detector electrodes through the pyroelectric effect and the magnitude of the charge change is given by:

$$\Delta q = p A_d \Delta T \quad (14)$$

where : Δq = charge change in coulombs
 p = pyroelectric coefficient in coulombs/K/cm²
 ΔT = temperature change in K
 d = detector area in cm²

Another mode of operation that has proved successful is the use of an electrically biased dielectric that undergoes a dielectric constant change as a function of temperature (T.I. system). The equations that pertain to this system are:

$$q_1 = C_1 V \text{ at temperature } T_1$$

$$q_2 = C_2 V \text{ at temperature } T_2$$

$$\Delta q = q_1 - q_2 = V(C_1 - C_2) = K_0(\epsilon_1 - \epsilon_2) = K_0 \Delta \epsilon \quad (15)$$

If we define a term $p_0 = d\epsilon/dT$ then:

$$q = K_0 p_0 \Delta T \quad (16)$$

and the analytic equations are essentially the same with slightly different physical meanings attributed to the figures-of-merit. The array does not transform the irradiance input into temperature (or voltage) perfectly, nor does the readout device transfer the voltages out of the array perfectly, so that an ideal display will show spatial distortions due to thermal spread between elements and to electrical transfer inefficiencies. In addition, electrical noise generated within the array elements and in the input circuitry will be added to the array element voltages. These noises are responsible for ultimately limiting the ability of the array to detect spatial variations in irradiance.

The ultimate goal of the electrical modeling is to characterize the performance of the array. We wish to model its spatial resolving capability, by use of the MTF, its noise limited sensitivity, by use of the noise equivalent irradiance or flux density (NEFD), and its irradiance-to-voltage transfer function, its responsivity.

Performance modeling of the array is to be referenced back to the radiation input field of the array. Thus the MTF is to be modeled in terms of the spatial frequency content of the output of the array compared to the spatial frequency content at the input surface of the array itself. The NEP is to be a measure of that radiant input to the focal plane surface which produces a signal at the output equal to the noise level in the output.

The thermal model described in the preceding section models all thermal processes and generates a volume average temperature for use in computing the detector output. In particular, the thermal model computes a temperature difference output signal, synchronized with the chopper motion. This quantity is the difference between the volumetric average temperature at the time when the chopper just uncovers the element and at the time it just recovers the element. It is computed for each element throughout the thermal modeling process. When converted to a voltage, this signal provides a rectified signal that is synchronized with the chopper motion. In actual detector arrays, this rectification process is performed in the array itself. This allows the simulation of the thermal details of the chopping process without requiring a detailed model for the rectification process of the readout.

These temperature differences can be used along with an overall model for the array to model the performance of the array in terms of the electrical signals at its output compared to its radiant input. The concepts of MTF, responsivity, and noise equivalent input all assume the existence of a linear relationship between the input irradiance and the output. Thus we have enforced a linear model throughout the analysis.

Electrical Modeling

The electrical modeling consists of the development of a model whereby the temperature differences computed in the thermal model can be converted to electrical outputs, and the modeling necessary to properly introduce the noise mechanisms in the array element and readout. The resulting model can then include the effects of various noise sources on the sensitivity of the device and on its spatial resolution.

The following discussion is based on the CCD readout structure used by HEOD. For modeling purposes, the radiation pattern is stationary in space except for an on/off modulation imposed by a chopper. The following characteristics are carried over from the HEOD structure [9].

- 1) The chopper has a 50 percent duty cycle; this is not a restriction of the thermal model.
- 2) If the chopper period is T and the readout device frame time is τ , then

$$2K\tau = T \quad (17)$$

where K is a selectable integer value from 1 to 16.

- 3) The CCD readout device used indirect charge injection at its parallel inputs, with an input structure something like that shown below in Figure 2.
- 4) All of the detector signals over the whole focal plane are multiplexed through a single output port as described below. Figure 3 shows the pattern of signal flow.

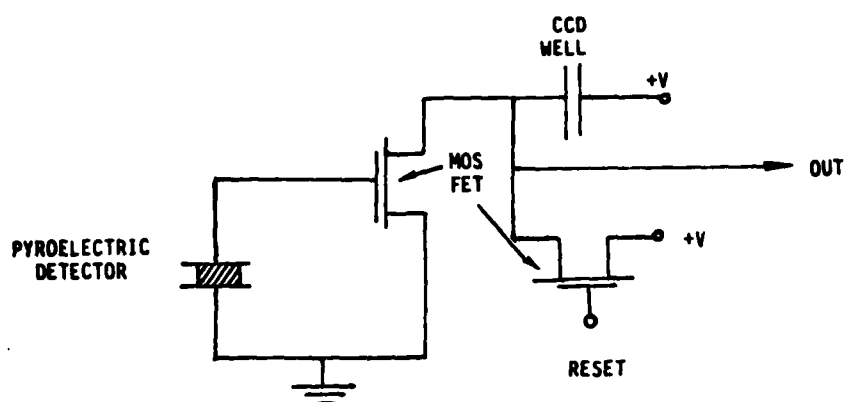


FIGURE 2. REPRESENTATIVE INDIRECT CHARGE INJECTION.

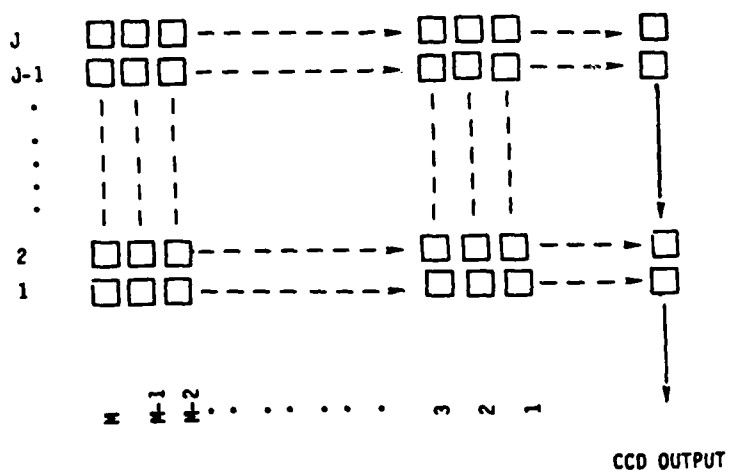


FIGURE 3. CCD DATA FLOW.

The readout cycle is as follows. The detector signals are parallel-transferred into the CCD structure of Figure 3, so that the $M \times J$ cells comprise an image of the detector signals integrated over a frame time. All of the signals are transferred to the right by one step (one cell width). Then the vertical CCD register at the extreme right is strobed until it has emptied all of its data into the output port. Another single step of the data to the right follows, the vertical CCD register is completely emptied, etc., until all of the data from the focal plane has been read out to the CCD output.

FOCAL PLANE OUTPUT VOLTAGES

The thermal analysis code calculates a composite change in detector temperature, ΔT , for each detector after each time step, Δt , specified for the finite difference thermal model. Without loss of generality, we can define the time t to be zero at the opening of the chopper (that is, the focal plane is first illuminated by the imposed radiation pattern at $t=t_0=0$). Also without loss of generality, we can specify the voltage across each of the detectors to be zero at $t=0$. For convenience, and also without loss of generality, the size of a time step Δt can be defined as an integer fraction of the frame time, τ :

$$\Delta t = \frac{\tau}{N}, \text{ where } N \text{ is an integer.} \quad (18)$$

Referring to the circuit of Figure 2, this same indirect charge injection circuit is modeled in a form which is appropriate for the necessary circuit analysis in Figure 4. In Figure 4, C_T is the sum of the detector capacitance, the MOSFET common source input capacitance and stray capacitance. R_T is the net leakage resistance shunting the detector.

During the n^{th} time step, the $(j,m)^{\text{th}}$ detector is shown by the thermal analysis code to have experienced a composite temperature change $\Delta T_{j,m,n}$. In response to that temperature change, the detector generates sufficient

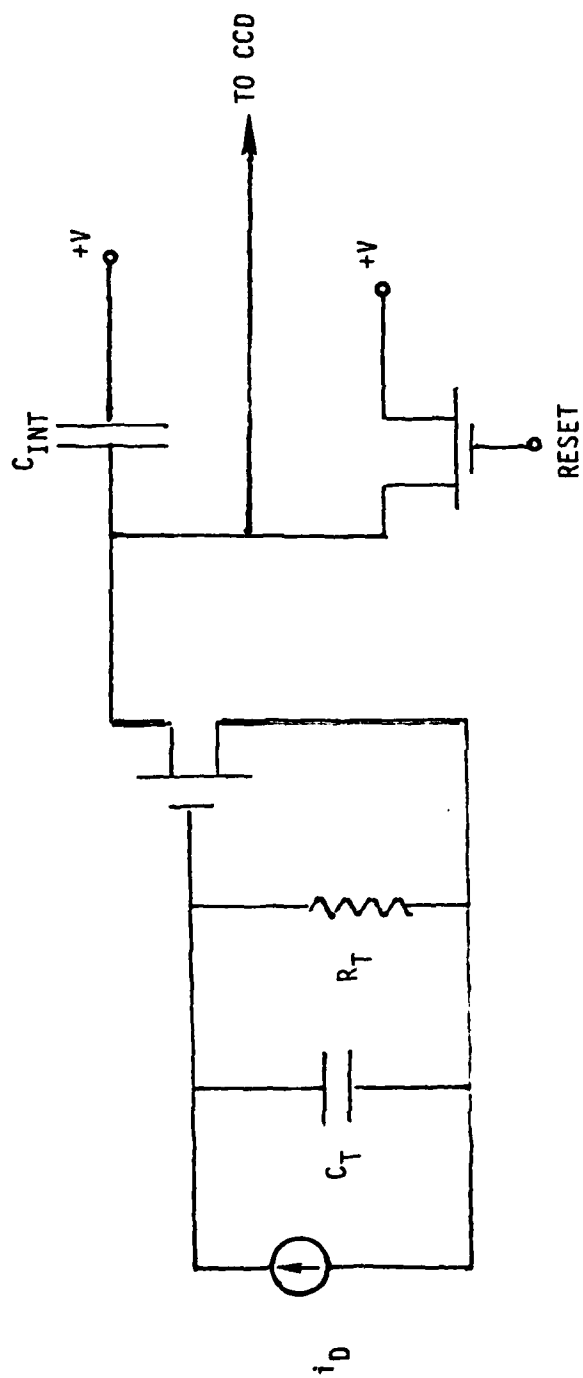


FIGURE 4. CIRCUIT OF CCD CHARGE INJECTION SCHEME.

displacement current through its dielectric that, over the corresponding time step of size Δt , a charge of Δq has been transported across the detector. Under the reasonable assumption that detector current is a piecewise linear function of time during any time step, the detector current $(i_D)_{j,m,n}$ is defines as:

$$(i_D)_{j,m,n} = a_{j,m,n} t \quad t_{n-1} < t \leq t_n \quad (19)$$

where

$$a_{j,m,n} = \frac{2}{(\Delta t)^2} \Delta g_{j,m,n} = \frac{2PA_D}{(\Delta t)^2} \Delta T_{j,m,n} \quad (20)$$

where P is the pyroelectric coefficient and A_D is the area of the detector. The voltage across the $(j,m)^{th}$ detector after the n^{th} time step is given by

$$V_{j,m}(t_n) = R_T a_{j,m,n} \Delta t - R_T^2 C_T a_{j,m,n} \left(1 - e^{-\frac{\Delta t}{R_T C_T}} \right) + V_{j,m}(t_{n-1}) e^{-\frac{\Delta t}{R_T C_T}} \quad (21)$$

This voltage also appears at the gate of a common source MOSFET associated with the $(j,m)^{th}$ detector. The drain current of this MOSFET is related to its gate voltage $V_{j,m}(t_n)$ by

$$i_{Drain} = g_m V_{j,m}(t_n) + A \quad (22)$$

where g_m is the MOSFET transconductance and A is the constant which is related to the MOSFET threshold voltage. Since the MOSFET transconductance is itself proportional to the square root of i_{Drain} , Equation 22 is nonlinear.

The charge which is actually injected into and transported through the CCD is the charge accumulated on C_{int} due to i_{drain} . At the beginning of each frame, the reset MOSFET is briefly strobed into the "on" state, so that the charge of C_{int} is initialized to zero. At the end of a frame, the discrete charge packet resulting from the integration of i_{drain} over the frame time is injected into the CCD readout structure where it subsequently will be transported to the CCD output. A sample-and-hold operation is typically performed at the output, thereby transforming the charge packet into a voltage analog. The operation is then repeated over the span of a subsequent frame.

Such detail regarding the CCD input structure might be considered to be beyond the scope of the TFPA study. However, two important pieces of information can be extracted from this operational detail. The first is that a signal representative of the integral of the detector signal over a frame time is the quantity transported through the CCD. Thus, the form of the detector outputs which must be provided to the CCD is known. It is simply the checkerboard image of the focal plane, wherein each detector signal is updated to the current value at the end of each frame. The second is that the indirect charge input structure has some undesirable characteristics. Most serious is the nonlinearity in Equation 22. The concept of an MTF is valid only for linear systems. HEOD's CCD structure, after which this exposition is patterned, incorporates an output compensation scheme which is intended to remove the signal nonlinearity. Because such a compensation scheme must operate upon the signals after they have been integrated over time, it is clear that the compensation scheme must inherently be imperfect.

Again, considering the scope of the TFPA study, we have little choice but to assume that the CCD throughout is linear. The user of the TFPA model should, however, be aware of its limitations. When the thermal calculations are performed at each finite-difference time step, Equation 21 can be updated for each detector with negligible additional computational load. After the end of a frame time, composed of N time steps, has been reached, the voltage across each detector in the focal plane has been determined.

One of the most important characteristics of the array is its MTF, which is a measure of the transfer of information through the array as a function of spatial frequency. Both thermal and electrical effects have an influence on the spatial transfer function. Since we are considering only rectilinear arrays with no thermal asymmetry in this development, the thermal portions of the MFT will be identical along the two dimensions of the array. Although it is highly probable that the two dimensional MTF (w_x, w_y) (where w_x and w_y are the spatial frequencies in the two orthogonal array dimensions) is not separable into independent one-dimensional MTF's, traditional modeling assumes such a separability, and for comparison with existing measurements, we have implemented only a one-dimensional MTF (although the thermal code could easily support a two-dimensional calculation if appropriate sources were introduced).

Consider the MTF for the thermal differences, ΔT , or its equivalent, the MTF of the individual array voltages. Referring to Figure 3, let us consider the MTF in the horizontal, or i^{th} , direction. A straightforward way to calculate the MTF of system 1 in the i^{th} dimension is to apply a stationary, spatially-sinusoidal radiation pattern to the focal plane having spatial frequency w_1 in the i^{th} dimension with complete uniformity in the j^{th} dimension. Because of the influence of the CCD readout device, the MTF exhibits a slight variation over the focal plane and so a specific row of detectors, say the J_1^{th} row, must be chosen for analysis. The detector signal values obtained from Equation 21 at the end of the first frame time, $V_{j_1, m}(t_n)$, must be Fourier transformed in space along the m^{th} dimension. As has been indicated by the integrate-and-transfer operation of the CCD, the detector signal form in space is a sequence of rectangular pulses with amplitudes corresponding to the real detector signal values in the j_1^{th} row and pulse width equal to the geometrical detector center-to-center spacing along the m^{th} dimension.

The spatially transformed sequence of detector signals is $F_1(w_1)$. Similarly, the same sinusoidal radiation pattern except with arbitrary spatial frequency w_k can be run through the thermal model and the resulting detector signals can be spatially Fourier transformed into $F_2(w_2)$. If the input radiation sinusoids

have the same amplitude, then the sequences of $F(w)$ form the MTF for the j^{th} row of detectors in the m -direction. In order to follow the usual definition of MTF, the spatial frequencies w_k are normalized to the Nyquist spatial frequency along the m -direction, i.e., 2π divided by the center-to-center detector spacing. Thus,

$$\text{MTF} = \left| \frac{F(w)}{F_0(0)} \right| \quad (23)$$

The function $F_0(0)$ must be computed from the temperature output from a completely uniform radiation field. However, the approach of putting one sinusoid (of one frequency) through the thermal model at a time is unnecessarily wasteful of computer resources. A much more reasonable approach is to apply a radiation function to the focal plane which contains all frequencies. Any waveform which contains a discontinuity, such as a step function, would do. However, the ideal radiation input waveform is a spatial delta function, since the Fourier transform of a delta function consists of all frequencies equally weighted. Thus, the spatial Fourier transform of the output of the J_1^{th} row of detector signals, resulting from a source consisting of a one-dimensional delta function, $F_{j_1}(w)$, can be used to formulate the MTF for the J_1^{th} row of detectors as a continuous function of normalized frequency.

$$\text{MTF}_{\text{focal plane, } j_1^{\text{th}} \text{ detector row}} = \frac{\left| F\left(\frac{w}{w_{\text{Nyquist}}}\right) \right|}{|F(0)|} \quad (24)$$

We can now proceed with a more general, less detailed model for the whole detector-readout system from which expressions for the system performance, in terms of the results of the thermal analysis, can be determined.

GENERALIZED MODELING

Despite the detailed discussion of the previous sections concerning the structure of readout mechanisms, chopper-synchronized differencing processes, and non-idealities in the readout systems, the wide differences between various array implementations make detailed treatment of the output processes of any individual design less than desirable. The resulting code would be too limited. To avoid the specialization of the code to any particular readout mechanism, we have designed a generalized model wherein noise contributions can be reasonably modeled and reasonably general expressions for responsivity, NEP and MTF, can be derived.

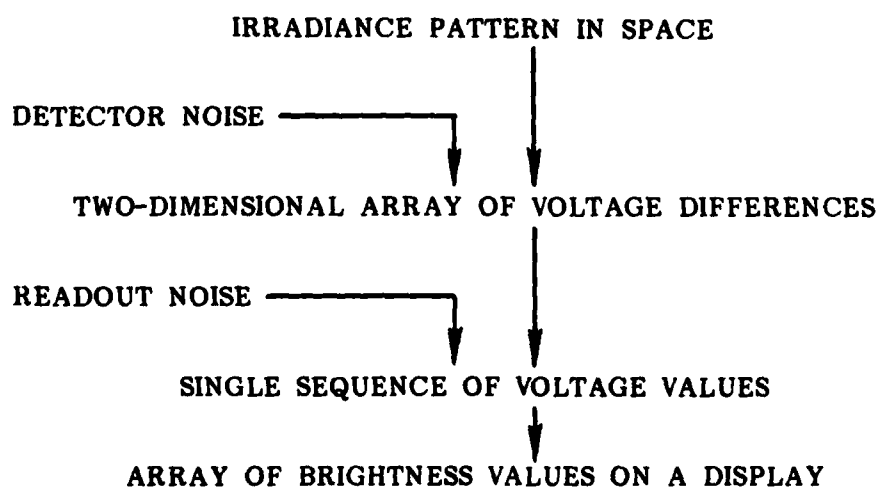
To this end, we have assumed that two linear system functions exist for the transformation of radiant input power from a static (temporally invariant) irradiance scene into the output voltages. (While the thermal model can handle general temporally varying scenes, the present formulation for MTF is restricted to time invariant patterns.) The first of these transfer functions is taken to encompass all processes of spatial integration, pyroelectric effects, and the actions of the chopper, including the signal detection process in synchronism with the chopper. Noise contributions include all those noises up to the extraction of a sample voltage level. Thus, the output of this first process consists of an array of voltage sequences, a three-dimensional function, two dimensions of which are the array spatial dimensions and the third of which is the sample sequence dimension, corresponding to time. Note that in the generation of these sequences, and in the modeling of the effects of the detector processes, no reference to time is needed; the detector outputs are simply discrete voltage outputs. The noises which contribute to this voltage sequence consist of all noise processes present in the array elements themselves. Since the detector elemental voltages are sampled to obtain the output voltage sequences, the expressions for the power spectra of the various noise contributions must be modified to account for the integration process, and the variance of the sampled noise computed.

The resulting sequences of signal voltages (and noise voltages) are then passed through the second process, the readout device, which orders the array of voltage sequences into a single sequence of voltages for passage out through

a single line. This process both distorts the signals and adds noise. These effects of the readout device contribute to both the degradation of spatial resolution and to the noise of the system.

The detector array signals form a matrix in space and a sequence in time, with the time duration of each element of the sequence chosen so that the whole array is read out in one frame period. The sequence of voltages is not itself examined in time, but is presumably used to generate an image of the array output for presentation to the user. Thus the spatial frequency content as apparent in the display of the array output is to be compared to the spatial frequency content of the radiant input. The time domain (for stationary scenes) plays only a very incidental role in such a process. Time is important only to the extent that it takes time to sample the array, order the array of voltages into a single line and present it to this display. Time is also important in that the noise processes of the detector elements and readout devices are specified in terms of temporal power spectral, which must be integrated to obtain sample statistics from temporal statistics.

Thus an overall model for the thermal focal plane array suitable for definition of typical performance parameters can be constructed as the following set of linear operations:



The vertical arrows represent the linear processes; the inserted noises represent the origination of noise contributions. Two noise contributions are important: those which originate in the detector elements themselves and those which originate in the readout device. Johnson noise, so-called "loss tangent" noise and noise due to thermal fluctuations are typical noises which originate in the detector. (Individual noises are considered in a later section.) Amplifier noise, reset noise and other electronic uncertainties constitute the contribution labelled readout noise. In the analysis presented here, all noise processes have been referenced to the readout input. Thus, all noises can be lumped together and assumed to originate at the detector. This means that the processes representing the readout and display processes can also be lumped together. Figure 5 shows a "black box" flowchart of these processes.

In this analysis, we have chosen to ignore all temporal variations in the input scene and assume the scene to be static. Our neglect of these variations is prompted by the required chopper system; it greatly complicates the treatment of temporally varying scenes.

The scene is considered static for this performance parameters (MTF and NEP) evaluation, so that only spatial variations are of interest. Within this limitation and in the spirit of other definitions, the MTF of the system will be defined as the filtering performed by the overall system on spatial information expressed in two-dimensional spatial frequency space.

NEP or NEFD or equivalently, noise equivalent irradiance is an expression of the radiant input required to give an output equivalent to the noise generated within the device. It can also be thought of as a function in two-dimensional spatial frequency space. The noise must be considered as the noise-generated frame-to-frame variations in the display device output.

Finally, the responsivity is a measure of the conversion of radiant energy into electrical signal, generally having units of volts/watt or volts/watt/cm². This can also be thought of as a spatial frequency dependent quantity and is generally equivalent to the transfer function of an individual detector element, i.e., the transfer function of the leftmost box in Figure 5. The commonly quoted value is the DC or zero spatial frequency value.

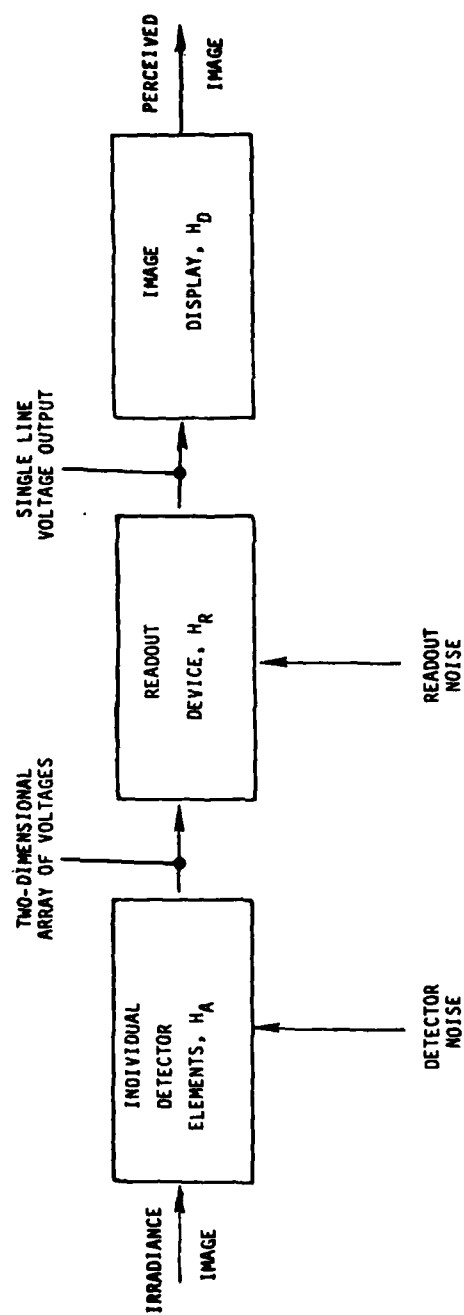


FIGURE 5. LINEAR MODEL OF TFFA DEVICES.

Each of the functions represented by boxes in Figure 5 is assumed to be a linear, spatially invariant process so that the actual output of each box can be represented as a convolution of its input with its transfer function in space. When this is the case, the output of each box in two-dimensional frequency space can be represented as the product of the (two-dimensional) Fourier transform of its input and the (two-dimensional) Fourier transform of its transfer function. The transformation between the physical space of the input scene and the two-dimensional array index space of the array is included in the convolution process. Similarly the transformation from the two-dimensional array space of the detector element to the one-dimensional output sequence and back to spatial display space is represented by a convolution process. The corresponding Fourier transforms give the relationships between the various frequency spaces.

The following equations develop these relationships in more detail in order that precise expressions for MTF, NEFD and responsivity can be developed in terms of the thermal code outputs, the array physical properties and the postulated readout characteristics.

The two-dimensional array of detector output voltages can be determined from the irradiance input image as follows:

$$V(i,j) = \int_{x'} \int_{y'} H_A(i\Delta x - x', j\Delta y - y') E(x', y') dx' dy' \quad (25)$$

Here H_A is linear process transducing the irradiance distribution $E(x,y)$ incident on the array into the i,j array of detector voltages. Note that H_A includes all chopper effects and all effects of detection area. x and y are the dimensions of an individual array element. Appendix C presents an initial description of the system including the details of the chopper operation.

This voltage signal is passed through a readout device and is then displayed as a two-dimensional display in which each element of the two-dimensional array of voltages is converted to an output value corresponding to the appropriate pixel. Thus although the image output consists of a discrete array of voltages, the frequency information can be kept in the spatial domain.

Furthermore, a continuous representation of detector voltages is preferable to the discrete representation. It avoids the problems associated with the conversion to and from the discrete space of the detector elements. The voltage as a continuous function of spatial position (Equation 25) can then be written in the spatial domain as

$$V(x,y) = \iint H_A(x-x',y-y') E(x',y') dx'dy' \quad (26)$$

In the spatial frequency domain, this becomes

$$V(w_x,w_y) = H_A(w_x,w_y) \cdot E(w_x,w_y) \quad (27)$$

where functional dependence on a pair of frequencies implies the application of a Fourier transform to the function. w_x and w_y are spatial frequencies in the x- and y- directions respectively. Thus

$$H_A(w_x,w_y) = \iint_{-\infty}^{\infty} H(x',y') e^{-i(w_x x' - w_y y')} dx'dy' \quad (28)$$

and similarly

$$E(w_x,w_y) = \iint_{-\infty}^{\infty} E(x',y') e^{-i(w_x x' - w_y y')} dx'dy' \quad (29)$$

$$V(w_x,w_y) = \iint_{-\infty}^{\infty} V(x',y') e^{-i(w_x x' - w_y y')} dx'dy' \quad (30)$$

$H_A(w_x, w_y)$ is the spatial frequency dependent responsivity function for the focal plane array alone, i.e., exclusive of the effects of the readout device. The so-called DC responsivity of the array is $H_A(0,0)$ and the MTF of the array is the amplitude of the response at any given frequency compared to that at DC. Thus, the magnitude of the responsivity, R_A is:

$$R_A(w_x, w_y) = |H_A(w_x, w_y)| \quad (31)$$

$$MTF_A(w_x, w_y) = \frac{|H_A(w_x, w_y)|}{|H_A(0,0)|} \quad (32)$$

$$|H_A(w_x, w_y)| = R_A(0,0) \cdot MTF_A(w_x, w_y) \quad (33)$$

The only effects of the readout device on the MTF that we have included in the present model are those of incomplete charge transfer between CCD cells. These effects are properly considered in a one-dimensional discrete domain. However, for the CCD systems to be used with these arrays, the transfer arrangement is such that all transfers in one direction are made before any in the other. Thus the smearing effects of charge transfer remain completely separated in the two dimensions, and the effects of a CCD on responsivity and MTF can be treated as simply the product of two independent effects, so that the overall MTF can be written:

$$MTF(w_x, w_y) = MTF_A(w_x, w_y) \cdot MTF_{CCD}(w_x) MTF_{CCD}(w_y) \quad (34)$$

The two CCD effects can be written [10]

$$MTF_{CCD}(w_x) = \exp \{I\epsilon_x [1 - \cos(w_x \Delta x)]\} \quad (35)$$

$$MTF_{CCD}(w_y) = \exp \{J\epsilon_y [1 - \cos(w_y \Delta y)]\} \quad (36)$$

where I and J are the number of transfers in the x- and y-directions respectively and ϵ_x and ϵ_y are the respective single stage transfer losses. Note that since $MTF_{CCD}(0) = 1$ for all values of $1/\epsilon_x$, the charge transfer inefficiencies do not contribute to the DC responsivity. Thus

$$R(0,0) = R_A(0,0) \quad (37)$$

$$R(w_x, w_y) = R(0,0) MTF_A(w_x, w_y) \cdot MTF_{CCD}(w_x) MTF_{CCD}(w_y) \quad (38)$$

$H_A(w_x, w_y)$ is obtained as the Fourier transform of $H_A(x', y')$, which is in turn determined from the output of the thermal code. First of all, to make the results of the code comparable to other modeling studies, we have made the common assumption that $H_A(w_x, w_y)$ is separable into two independent one-dimensional contributions for the x and y coordinates respectively. By making this assumption, we can use a line source to represent a delta function source in one dimension and use it to probe the response function of an array element in that direction. Note that an integral over a delta function can be viewed as "pulling out" the value of the remainder of the integrand at the point where the delta function is applied. Thus the use of a delta function in irradiance as input to the thermal code can be used to determine values of $H_A(x)$ as a function of x. Under the separability assumption

$$H_A(w_x, w_y) = H_{A_x}(w_x) H_{A_y}(w_y) \quad (39)$$

and with the use of a line source in the y-direction at the position x_0 , i.e.,

$$E(x, y) = E_y \delta(x - x_0) \quad (40)$$

where E_y is the irradiance of the line source per unit source length, we obtain from Equation 25,

$$V(i, j) = \int_{x'} \int_{y'} H_A(i\Delta x - x', j\Delta y - y') E(x', y') dx' dy' \quad (41)$$

$$= E_y \int_{-\infty}^{\infty} H_A(i\Delta x - x_0, j\Delta y - y') dy' \quad (42)$$

or in terms of a separable H :

$$V(i) = \int_{-\infty}^{\infty} H_{A_y}(u) du \cdot H_{A_x}(i\Delta x - x_0) \cdot E_y \quad (43)$$

(Index j becomes irrelevant here since all elements j will see identical results.) The output of the thermal code is used to determine $V(i)$ for various positions, x_0 , of the input delta function source. Then H_A can be determined from

$$H_{A_x}(i\Delta x - x_0) = \frac{V(i)}{E_y} \frac{1}{\int_{-\infty}^{\infty} H_{A_y}(u) du} \quad (44)$$

or by simply changing variables,

$$H_{A_x}(x') = \frac{V\left(\frac{x' + x_0}{\Delta x}\right)}{E_y} \frac{1}{\int_{-\infty}^{\infty} H_{A_y}(u) du} \quad (45)$$

Note that the integral of the response in the y-direction over the whole y-direction is a constant in this determination of the x-direction response.

A determination of the response in the y-direction can be performed similarly but with the line source in the x-direction. With present thermal code, this is not generally done since it is simpler to turn the array and perform another set of calculations. Furthermore, if the array elements are square, there is no need to run a second direction; the isotropy of the materials ensures identical results.

The DC responsivity of the system is simply the integral of $H_A(x,y)$ over all space x and y. Within the separability assumption, the responsivity at DC can be determined from Equation 45 as:

$$R(0) = \int_{-\infty}^{\infty} H_{A_x}(u) du \cdot \int_{-\infty}^{\infty} H_{A_y}(v) dv = \frac{\int_{-\infty}^{\infty} V(x) dx}{E_y} \quad (46)$$

The responsivity is simply the integral of the output voltage translated into space divided by the line source intensity in watts/cm. Note that the responsivity can be obtained from results in only one direction.

Furthermore, the MTF function can be obtained from a Fourier transform of $V(x)$, normalized to its zero frequency value.

$$MTF_x(w_x) = \frac{|V(w_x)|}{|V(0)|} \quad (47)$$

To obtain an MTF in one direction, it is not necessary to obtain a value for the integrated response function in the other direction.

Formulation of Noise Components, NEP and D^* for Pyroelectric Detector/CCD Readout

Such important system parameters as NEP and D^* depend upon appropriate formulations of system noise. The following is the formulation of relevant noise sources as well as formulation of NEP and D^* expressions. The noise equivalent model of the system is shown in Figure 6.

Noise is introduced into this system by the sampling of the time dependent noise generated both in the detector elements and in the input stages of the system electronics. The sampling of this noise leads to uncertainties in the output voltage array which vary from frame-to-frame. Thus, the noise in the system can be characterized by the temporal noise power spectrum of each of the noise contributions, which can be added to yield a total noise spectrum. The composite noise as it appears in the system output is characterized by this composite noise spectrum as integrated over a sample time. The noise passes only through the readout device; therefore the only frequency content modifications are made by that device.

We assume that all noises can be referenced to the detector output. HEOD [9] has advised us that the MOSFET used for indirect charge injection into their CCD has sufficient gain that noise sources downstream of the MOSFET can be ignored. Similarly, we assume that noise sources downstream of the TI multiplexer can wither be referenced to the multiplexer input or ignored. Thus,

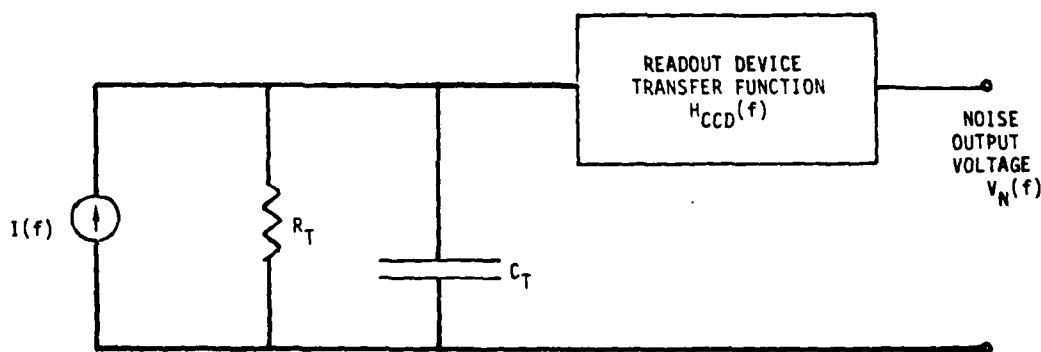


FIGURE 6. SYSTEM NOISE EQUIVALENT MODEL.

the noise current power spectra can be summed in quadrature into a single noise power spectrum. So

$$I(f) = \left[\sum_i I_i^2(f) \right]^{1/2} \quad (48)$$

and the components of $I(f)$ are defined to be:

I_1 = Johnson noise current of R

$$= \left(\frac{4kT}{R_T} \right)^{1/2} \frac{\text{amp}}{\sqrt{\text{Hz}}} \quad (49)$$

I_2 = radiation noise current

$$= (16 k \sigma T^5 A_d \epsilon) \frac{1}{C^2 d} \frac{\text{amp}}{\sqrt{\text{Hz}}} \quad (50)$$

I_3 = Johnson noise of detector dielectric

$$= \frac{1}{\sqrt{d}} (8\pi k T A_d \epsilon' \epsilon_0 f \tan \delta)^{1/2} \frac{\text{amp}}{\sqrt{\text{Hz}}} \quad (51)$$

I_4 = Statistical noise due to discrete nature of gas conduction between detectors

$$= \left(4kT^2 K A_d \right)^{1/2} \left(\frac{4\pi f}{k_g} \right)^{1/4} \frac{1}{C^2 d} \frac{\text{amp}}{\sqrt{\text{Hz}}} \quad (52)$$

I_5 = Statistical noise due to lateral thermal conduction

$$= \frac{1}{C^2} \left(\frac{4kT^2 K_p}{d} \right)^{1/2} \left(\frac{4\pi^2 f A_d}{k_p} \right)^{1/4} \frac{\text{amp}}{\sqrt{\text{Hz}}} \quad (53)$$

I_6 = Equivalent input noise current of indirect charge injection input MOSFET

$$= \text{user specify } \underline{\text{default}} \rightarrow 5 \times 10^{-17} \frac{\text{amp}}{\sqrt{\text{Hz}}} \quad (54)$$

I_7 = The equivalent of input noise voltage of input MOSFET

$$= \frac{B}{|Z|} \left(\frac{1}{f} + \frac{1}{f_o} \right)^{\frac{1}{2}} \quad (55)$$

where:

k = Boltzmann's constant = 1.38×10^{-23} (watts-sec/K)

σ = Stefan-Boltzmann constant = 5.67×10^{-8} (watts/m²-K⁴)

T = Detector nominal temperature (Kelvin)

R_T = Net leakage resistance across detector

R_T = User specify default $\rightarrow 10^{13}$ (Ω)

A_d = Detector area (m²)

α = Absorptivity of detector active surface

P = Pyroelectric constant (Q/m²-K)

C' = volumetric specific heat (J/m³-K)

d = Detector thickness (m)

ϵ' = Real part of detector relative dielectric constant

ϵ_o = Free space dielectric constant = 0.111×10^{-9} (Farad/m)

f = electric frequency (Hz)

$\tan \delta$ = Dielectric loss factor

K = Thermal conductivity of gas surrounding detectors
(watt/m-K)

k_g = Thermal diffusivity of gas surrounding detectors (m²/s)

K_p = Thermal conductivity of detector material (watt/m-K)

k_D = Thermal diffusivity of detector material (m^2/s)

$|Z|$ = Steady-state value of parallel impedance across detector (Ω)

$$= \frac{R_T}{[1 + (2\pi f R_T C_T)^2]^{1/2}} \quad (56)$$

where: C_T = Total parallel capacitance across detector (Farad)

$$= C_D + C_S \quad (57)$$

C_D = Detector capacitance (Farad)

$$= \frac{\epsilon' \epsilon_0 A_d}{d}$$

C_S = Total parallel stray capacitance (Farad)

$$= \text{User specify default} \rightarrow 0.15 \times 10^{-12} \text{ Farad}$$

$$B = 10^{-6} \left(\frac{30 f_o}{30 + f_o} \right)^{1/2} \quad (58)$$

where: f_o = Corner frequency of input MOSFET $1/f^{1/2}$ noise

$$= \text{User specify default} \rightarrow 30 \text{ Hz}$$

The noise generated at the input of the CCD is that uncertainty resulting from the integration and sampling of the noise spectrum, resulting in a single random quantity for each voltage measurement. We can reasonably assume that these sampled noise voltages will be uncorrelated if the array has a reasonably large number of elements. When the number of elements is large, the time between each sample from any one element must then be larger than a single sample time, and if the appropriate filtering has been performed in the input stages to eliminate having time correlations much larger than a sample time, then the samples will indeed be uncorrelated. Of course, this assumption requires the presence of such low pass filtering and subsequent sections include such filtering, but we will ignore correlations between noise samples in the analysis that follows. These uncorrelated noise samples are associated with

individual elements of the output voltage array, and the spatial power spectrum of the noise input to the readout structure is simply the variance of these noise currents samples, multiplied by the square of the parallel input impedance across the detector, and by the sine squared x over x squared spatial dependence determined by the rectangular array elements. We obtain the following form for the noise spatial power spectrum as seen in the output device:

$$V_I(w_x, w_y) = 2\sigma_I^2(\Delta t) Z^2 \Delta x \Delta y \left[\frac{\sin \frac{w_x \Delta x}{2}}{\frac{w_x \Delta x}{2}} \right]^2 \left[\frac{\sin \frac{w_y \Delta y}{2}}{\frac{w_y \Delta y}{2}} \right]^2 \quad (59)$$

where $\sigma_I^2(\Delta t)$ is the variance of a composite noise current sample taken over time Δt . The determination of $\sigma_I^2(\Delta t)$ will be discussed subsequently. The factor of 2 arises because each output value results from two voltage measurements, one from each state of the chopper.

The effect of the readout structure is to modify the noise power spectrum in spatial frequency by the MTF of the CCD structure. Thus,

$$V_N^2(w_x, w_y) = 2\sigma_I^2(\Delta t) Z^2 \left[\frac{\sin \frac{w_x \Delta x}{2}}{\frac{w_x \Delta x}{2}} \right]^2 \left[\frac{\sin \frac{w_y \Delta y}{2}}{\frac{w_y \Delta y}{2}} \right]^2 \Delta x \Delta y \cdot \left| \text{MTF}_{\text{CCD}}(w_x) \right|^2 \cdot \left| \text{MTF}_{\text{CCD}}(w_y) \right|^2 \quad (60)$$

The NEP of the system is defined as that radiant input required to produce an output amplitude just equal to the noise amplitude at the system output. Equation 60 gives the output in terms of the radiant input. Equating the output from a source $\text{NEP}(w_x, w_y)$ to the noise output yields the appropriate expression

$$\begin{aligned}
 \text{NEP}(\omega_x, \omega_y) &= |H_A(\omega_x, \omega_y)| \cdot \text{MTF}_{\text{CCD}}(\omega_x) \text{MTF}_{\text{CCD}}(\omega_y) \\
 &= 2^{1/2} \sigma_I |Z| \Delta x \Delta y^{1/2} \cdot \left| \frac{\sin \omega_x \Delta x}{\omega_x \Delta x} \right| \cdot \left| \frac{\sin \omega_y \Delta y}{\omega_y \Delta y} \right| \\
 &\quad \cdot \text{MTF}_{\text{CCD}}(\omega_x) \cdot \text{MTF}_{\text{CCD}}(\omega_y)
 \end{aligned}
 \tag{61}$$

or

$$\begin{aligned}
 \text{NEP}(\omega_x, \omega_y) &= \frac{2^{1/2} \sigma_I |Z| \Delta x \Delta y^{1/2} \left| \frac{\sin \omega_x \Delta x}{\omega_x \Delta x} \right| \left| \frac{\sin \omega_y \Delta y}{\omega_y \Delta y} \right|}{|H_A(\omega_x, \omega_y)|} \\
 &= \frac{2^{1/2} \sigma_I |Z| \Delta x \Delta y^{1/2} \left| \frac{\sin \omega_x \Delta x}{\omega_x \Delta x} \right| \left| \frac{\sin \omega_y \Delta y}{\omega_y \Delta y} \right|}{R \cdot \text{MTF}_A(\omega_x, \omega_y)}
 \end{aligned}
 \tag{62}$$

This is the amplitude spectrum of the noise equivalent power in the spatial frequency domain, and represents the radiant input at any spatial frequency required to reproduce the noise amplitude apparent between individual frames, at that spatial frequency. Thus the temporal bandwidth of this NEP spectrum will be that associated with the frame time of the array. The total NEP is just

the DC radiant input required to produce the (spatial) variance in output, and is thus the integral of the noise spectrum over all spatial frequencies divided by the DC responsivity, thus

$$NEP_{total} = \frac{2^{1/2} \sigma_I |Z|^2}{R} \cdot \left[\Delta x \int_0^\infty \left(\frac{\sin \frac{w_x \Delta x}{2}}{\frac{w_x \Delta x}{2}} \right)^2 |MTF_{CCD}(w_x)|^2 dw_x \right]^{1/2} \cdot \left[\Delta y \int_0^\infty \left(\frac{\sin \frac{w_y \Delta y}{2}}{\frac{w_y \Delta y}{2}} \right)^2 |MTF_{CCD}(w_y)|^2 dw_y \right]^{1/2} \quad (63)$$

Note that the spatially dependent NEP is not constant with spatial frequency. Thus, the NEP will not generally be the same if the power were to be applied, say, over a square pattern and over a long, narrow rectangular pattern. It would not even be the same if the power were to be applied over two square patterns of different sizes. Such quantities as noise-equivalent temperature (NE Δ T) and minimum resolvable temperature (MRT) would similarly be associated with specific spatial patterns of radiation.

Values for D* can be computed for the system as follows. To the extent that the thermal focal plane array has absorptivity which is spectrally uniform, then D*_{blackbody} = D* _{λ} * = D* is formulated as

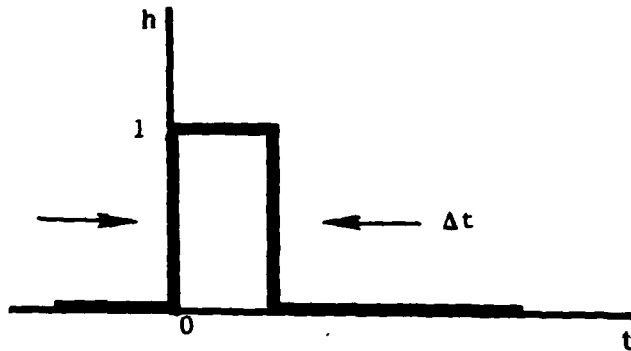
$$D^* (w_x, \text{system bandwidth}) = \frac{A_d^{1/2}}{NEP(w_x)} = \frac{(\Delta x \Delta y)^{1/2}}{NEP(w_x)} \quad (64)$$

$$D^*(\omega_y, \text{system bandwidth}) = \frac{A_d^{1/2}}{NEP(\omega_y)} = \frac{(\Delta x \Delta y)^{1/2}}{NEP(\omega_y)}$$

Finally, it is necessary to determine $\sigma_I^2(\Delta t)$. The noise current spectrum is the sum of the noise current spectra of each of the contributions, I_i , described earlier. Since the noise contributions all have a mean of zero, the mean value of the noise sample will also be zero. But the variance of the noise sample will depend on the temporal noise spectrum and the time over which the integral is taken. A value for the variance can be determined by noting that integration over a time interval Δt is equivalent to integration over a unit step function of duration Δt

$$v_{int} = \frac{1}{\Delta t} \int_{-\infty}^{\infty} \hat{h}(t-t') v_u(t') dt' \quad (65)$$

where $h(t)$ is a unit step of duration Δt , i.e.,



But the effect of this step function on the power spectrum is to multiply it by $[(\sin w\Delta t/2)/(w\Delta t/2)]^2$. Thus

$$S_{V_{int}}(w) = S_{V_u}(w) \left(\frac{\sin(w\Delta t/2)}{w\Delta t/2} \right)^2 \quad (66)$$

Furthermore, the variance of a function is just the integral of its power spectrum over all frequencies. In terms of the summed noise spectra $I(f)$

$$\sigma_I^2(\Delta t) = \int_0^\infty I^w(w/2\pi) \left(\frac{\sin w\Delta t/2}{w\Delta t/2} \right)^2 dw \quad (67)$$

(The $I_i(f)$ functions are all single-sided power spectra.) To determine $\sigma_I^2(\Delta t)$ in the code, first a set of w values are selected based on Δt . They have been chosen to properly cover the spectral range between DC and $4\pi/\Delta t$.

In practice, we have incorporated an additional low pass filtering operation to eliminate all noise substantially below the chopping frequency of the system. This is accomplished by the multiplication of $I(f)$ by a filter having a nominal cutoff at one-half the chopping frequency. Thus

$$\sigma_I^2(\Delta t) = \int_0^\infty \left(\frac{2w/w_c}{1 + 2w/w_c} \right)^2 I^2(w/2\pi) \left[\frac{\sin(w\Delta t/2)}{w\Delta t/2} \right]^2 dw \quad (68)$$

where w_c is the chopping frequency. This low pass filtering operation will prevent very low frequency noise from contributing to σ_1^2 when in practice it would be filtered out of the system. It will also help to insure that adjacent samples from any one detector will be uncorrelated.

Note that the use of the quantity $\sigma_1^2(\Delta t)$ as representing the detector noise contribution signifies the transformation of the electrical noise generated within the detector element (and of other input processes referenced back to the input) into discrete voltage samples which are then passed through the discrete CCD system and a discrete element output. Thus the discrete independent noise values are smeared by the CCD operations and mapped onto the display. The spatial spectrum of the independent noise samples is now given by the spatial spectrum of the array (or equivalently of the display) as modified by passage through the CCD.

In summary, the electrical portion of the code acts like a postprocessor, using a series of line sources at several positions to probe the lumped impulse response function of an individual detector element. The MTF of the array is determined by the spatial Fourier transform of this sampled impulse response. The responsivity is determined from the integration of this impulse response over the probed dimension. The noise of the system is modeled using a variety of contributions to detector element noises, plus the input noises referenced to the detector element outputs.

Finally, the spatial frequency dependent NEP and D^* values are computed from the responsivity, MTF and a sampled noise variance value computed using the composite detector noise spectrum. The total NEP is based on the signal necessary to produce the total output variance.

SECTION 5. CODE DESCRIPTION

The thermal focal plane array code has three main parts:

1. The Preprocessor produces an efficient set of input for the thermal calculations given the array configurations, dimensions and materials.
2. The Processor calculates the transient three-dimensional temperature distribution in array given inputs from preprocessor and boundary condition specification (radiative, convective and conductive). It also calculates voltage outputs of all detectors as a function of time given their electrical and pyroelectric properties.
3. The Postprocessor evaluates various detector performance parameters from the calculated voltage responses (generally for specific boundary conditions and configurations treated in the processor and preprocessor respectively) considering various thermal, electrical and signal processing noise sources.

Each of these components is discussed in order in the following three subsections. The numerical procedures and approximations will be discussed in detail.

5.1 PREPROCESSOR

The only purpose of the thermal focal plane array preprocessor is to set up input files for the processor and postprocessor. This module removes most of the effort in setting up the finite difference node structure and heat transfer paths, and optimizes the files for maximum computational efficiency in the processor.

The governing differential equation (Equation 1) is expanded in finite difference form [6] to give for an arbitrary node:

$$\rho C_p V [T(t+\Delta t) - T(t)] = \Delta t \sum_{i=1}^n \dot{Q}_i \quad (69)$$

where $\rho C_p V$ is the volumetric heat capacity of the node (e.g., J/K); T is the node temperature at discrete time points (e.g., t , $t+\Delta t$, $t+2\Delta t$, ...); and \dot{Q}_i are the net heat transfer rate to the node (e.g., J/s) from various sources ($i = 1, 2, 3, \dots$). These heat transfer terms may be due to only heat conduction (e.g., for internal

nodes), or can be due to combinations of conduction, radiation and convection (e.g., for surface nodes). The conduction terms are expressed simply as finite difference in space:

$$\dot{Q}_{\text{cnd}} = kA \left[\frac{T_i(t) - T_j(t)}{\Delta x_{ij}} \right] \quad (70)$$

where k is the thermal conductivity of the material between the i and j nodes, A is the cross-sectional area of the conduction path and Δx_{ij} is its length.

Note that this expression evaluates the heat transfer based on the temperature gradient at the start of the time interval (i.e., at t). This approximation introduces the usual finite difference errors and instabilities, but for the check cases we considered in the validation (see Section 6), these do not appear to cause problems for the temporal and spatial computational step sizes used. Other implicit techniques do not have these potential problems, but require more complex numerical procedures and so were not used in this initial version of the simulation code.

The preprocessor automatically subdivides the detector elements and surrounding materials into a three-dimensional orthogonal grid of nodes whose temperatures are to be calculated by the processor. These nodes are regularly spaced in each material, but arbitrary fineness of nodes can be specified for each material and each direction within the practical storage and run time limitations of the computer. Note that spatial resolution in the calculation influences temporal step size because of calculational stability considerations.

The preprocessor also automatically evaluates the effective path conductance for all paths connecting all nodes:

$$K_{ij} = kA/\Delta x_{ij} \quad (71)$$

The effective value calculated for paths between different materials considers the different material properties but neglects any contact resistance between the materials. The code then produces files for the processor containing the effective conductances for each path, the identification of the node pairs associated with each path, and the total heat capacity of each node:

$$C_i = \rho C_p V \quad (72)$$

Actually, the files contain "pointers" to efficiently specify the conductance K and capacity C . This is done because many of the paths will have the same value of K , and many of the nodes will have the same value of C . For example, all interior nodes in the detector may have a capacitance value $C(n)$ while all interior nodes in the insulation in some region may have a value $C(m)$. Then the files only need to specify the indices or pointers, n , m , etc., along with tables of $C(j)$, etc.

The radiative heat rates to all the irradiated surface nodes is approximately by:

$$\dot{Q}_{rad} = \alpha A E + \epsilon A \sigma (T_b^4 - T_i^4) \quad (73)$$

where α is the absorptance of the surface, A is the surface area of the node, E is the irradiance on the node (e.g., $J \cdot m^{-2} \cdot s^{-1}$) due to the focused infrared radiation that is to be measured, ϵ is the emittance of the surface, σ is the Steffan-Boltzmann constant, and T_b is the effective temperature of the radiative environment including everything except the focused radiation. This assumes that all the surface nodes exchange radiative energy with the same constant and uniform background.

The preprocessor automatically specifies the nodes that are on this irradiated surface, and calculates tables of radiative exchange factors for each node type (e.g., detector node, insulator nodes):

$$F_r = \alpha A \quad F_e = \epsilon A \sigma \quad (74)$$

These values are again specified by pointers for the sake of storage efficiency.

The other exterior surfaces of the detector element that are not irradiated by focused radiation may also exchange heat with their environment by radiation. For example, some configurations may have the detectors fully reticulated, but not backfilled with insulation, so nodes on adjacent detectors may transfer heat by radiation. Exchange factors for these nodes are automatically calculated by the preprocessor based on Equation 11:

$$F_S = A_1 F_{12} \quad (75)$$

This treatment assumes that the net radiative heat transfer to side surface nodes (i.e., not irradiated by focused radiation) is influenced only by the directly opposing node on the adjacent detector. The net radiation from all other sources is assumed to be zero; that is, on the average all other surfaces supply as much energy as they absorb (so-called "refractory" surfaces). The preprocessor automatically specifies the radiatively interacting node pairs, either between directly opposing nodes on adjacent detectors, or between nodes on the "bottom" surface of the detector and the substrate.

Convective heat transfer to surface nodes is also handled in a similar fashion. Using Equation 8, the code calculates convective exchange factors for all pertinent nodes.

$$F_C = Ah \quad (76)$$

This treatment assumes the ambient gas is an infinite heat source since its temperature never changes. The correlation used as input is based on measurements in air, but any convective coefficient can be specified as input.

The preprocessor also calculates a table of surface node positions. Currently, each position is given in terms of one coordinate only since this is how the irradiance function E is currently specified in the processor. Extension to two-dimensional irradiance patterns would require two coordinates to be transferred for each irradiated surface node.

Other output files are also prepared for the postprocessor. These files contain the configuration of the array, the area of the detectors and the position of the irradiated detector.

5.2 PROCESSOR

The processor reads the inputs from the preprocessor along with the parameters that specify the boundary conditions, and calculates the temperature of all the nodes at each time step. This calculation is carried out by simply evaluating the heat transfer for each path. The resulting temperature changes of the nodes for each path are accumulated, and after all the paths have been considered the new temperature of each node is evaluated from their initial temperature and net temperature change. These calculations are performed for as many time steps as desired within the computer run time limitations.

The processor also evaluates the volumetric average temperature of all the nodes in each detector at specified time increments. Since all the nodes in the detectors have the same volume, the volumetric average is simply the arithmetic average of all the node temperatures. The voltage output of the detectors is directly related to the difference in the volumetric average temperature at the beginning and end of the chopping cycle. These voltages as a function of time for each detector are stored in a file for further analysis in the postprocessor.

5.3 POSTPROCESSOR

The purpose of the postprocessor is to simulate the readout and signal processing functions of the thermal focal plane array system, and to evaluate the performance of the system in terms of various criteria. All the equations for the noise terms (see Section 4.2) are straightforward algebraic expressions that present no problem for computer evaluation. Similarly the expressions for the performance parameters are also straightforward. The only problem comes in evaluating the parameters at low chopping frequencies where the thermal solution requires large amounts of computer time. However, no special numerical techniques are required in the postprocessor. The postprocessor calculates the one-dimensional normalized MTF of the focal plane array as a function of spatial frequency using the predicted voltage response to a line source input as described in Section 4.2. This calculation involves a numerical

integration of the voltage over the line of detectors set up in the preprocessor for this calculation. The MTF for the imperfect charge transfer processes in the CCD are then evaluated and their product formed for determining the total MTF.

The postprocessor then evaluates the sum of the squares of the various noise currents as described in Section 4.2, and numerically integrates this sum over the spatial frequency range of interest. The evaluation of the noise currents is a simple matter of evaluating algebraic equations given in Section 4.2. The detector responsivity is then evaluated from the zero frequency MTF divided by the incident radiant power. Finally, the NEFD, NEP and D^* are calculated from the sum of the noise and the responsivity and other available detector parameters.

SECTION 6. CODE VALIDATION

Validation of the TFPA code proceeded by running check cases whose results were either compared quantitatively to results from analytic expressions or studied qualitatively for anticipated results. Check Cases A through D involved the heating of detector slabs by either a constant temperature boundary or a constant irradiance. Check Cases E through J had detector materials heated by modulated irradiances. All check cases and their results are described below.

CHECK CASES A THROUGH D

Check Cases A through D modeled detector slabs whose temperature changes were caused by constant irradiances or constant temperature boundaries. The temperatures within the slabs were compared to temperatures generated from theoretically produced analytic expressions. Each case is discussed below.

Check Case A

The initial check case considered the constant heating of a single detector whose temperature was assumed uniform at all times (the so-called "lumped approximation"). The radiative and convective heating were neglected and the pedestal and insulation were assumed to have negligible thermal conductivity so that the detector was effectively insulated. The detector was heated by a constant irradiation E_0 incident on the top surface.

The temperature T for this detector as a function of time (t) was calculated by the code and compared to the theoretical temperatures given by the analytic expression:

$$T(t) = T(0) + E_0 A t / CV$$

where: $T(t)$ = Detector temperature (Kelvin)

t = Time (seconds)

E_0 = Mean irradiance (w/m^2)

A = Irradiated surface area (m²)

C = Volumetric heat capacity (J/m³-K)

V = Detector volume (m³)

The temperature rise will be in K when E₀ is in watts/m². This expression shows that for a constant irradiance E₀, the change in the temperature of the detector should be linear with time. Run A showed that the code produced the same temperature and time relationship that theory predicts.

Using typical dimensions and thermal properties, a one-noded detector was heated by a constant 0.05 w/m² irradiance for 1 msec in 10 μs time steps. The code generated the identical linear temperature versus time relationship as did the theoretical expression (see Figure 7).

Check Case B

Check Case B introduced one-dimensional conduction by considering the thermal relaxation of the detector material which was assumed to be uniform initially at temperature T₀. Then the temperature of the bottom surface was suddenly raised to, and held steady at, another temperature T_f. Transverse conduction was neglected by using perfect insulation around the detector. The top surface was also perfectly insulated by setting the incident irradiation, radiative losses, and convective losses to zero. The exact solution for the comparison of code generated temperatures for this problem is given by Carslaw and Jaeger [11] as:

$$\frac{T(z,t)}{T(L,t)} = 1 - \frac{4}{\pi} \sum_{n=0}^{\infty} \left\{ \frac{(-1)^n}{(2n+1)} \exp \left[-(2n+1)^2 \left(\frac{\pi^2}{4} \right) \left(\frac{kt}{L^2} \right) \right] \cdot \cos \left[(2n+1) \left(\frac{\pi}{2} \right) \left(\frac{z}{L} \right) \right] \right\} \quad (78)$$

where K is the thermal conductivity (w/m-K), t is time (seconds), L is the total thickness (meters), and z is the vertical distance (meters) from the z=0 boundary at the top to the point of interest within the detector. Run B, which is

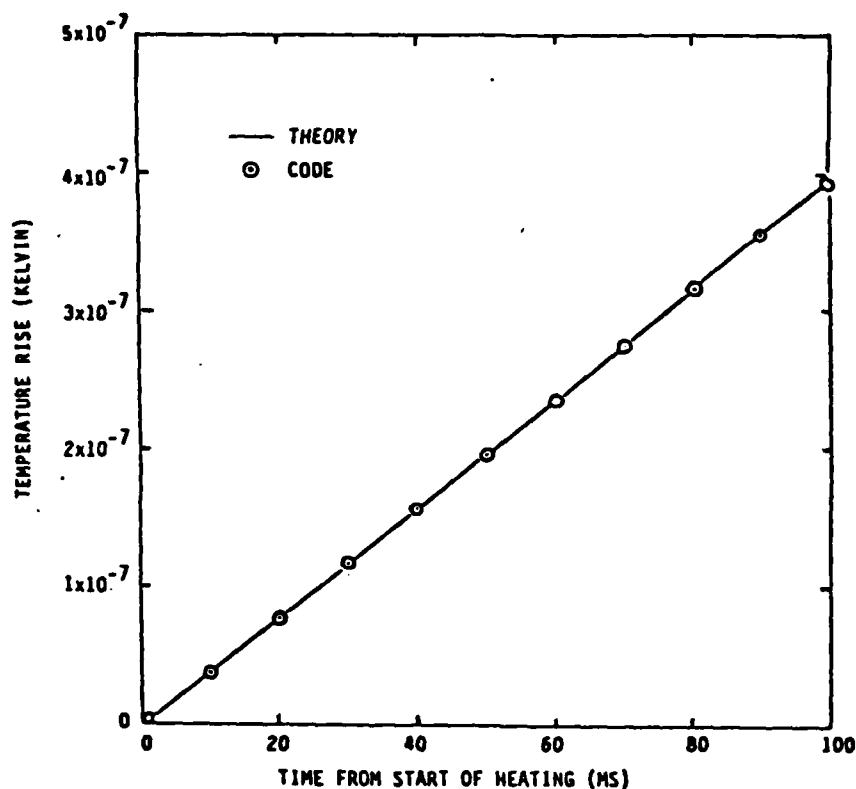


FIGURE 7. TEMPERATURE HISTORY OF AN INSULATED, THERMALLY LUMPED DETECTOR (HEAT CAPACITY OF 1.32×10^{-6} J/K) UNDER CONSTANT IRRADIANCE (0.05 W/M^2) ON AREA OF $1.03 \times 10^{-8} \text{ M}^2$, CHECK CASE A.

described below, produced temperatures in excellent agreement (see Figure 8) with those predicted by the exact expression above.

In Code Run B, the pedestal and detector were given identical dimensions and thermal properties and divided into ten layers each so that a detector slab with 20 layers was modeled. The initially isothermal detector was set upon a constant, slightly elevated, temperature boundary, the substrate. The detector was heated from the constant temperature substrate for 1 ms in 10 μs , time steps. The code generated temperatures that are in excellent agreement, (i.e., indistinguishable from theory on scale shown, see Figure 8) with those predicted by the exact expression above.

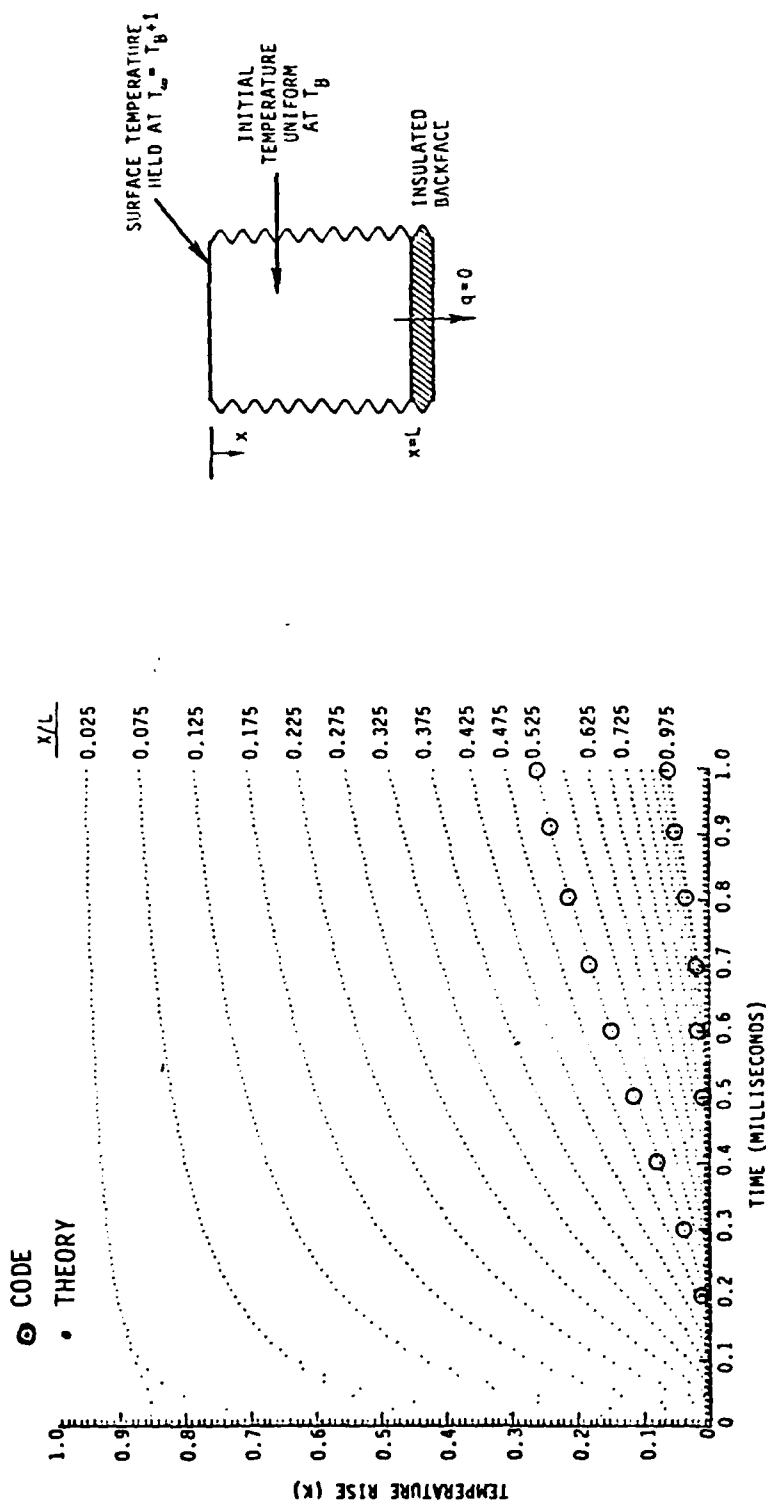


FIGURE 8. COMPARISON OF THERMAL FOCAL PLANE ARRAY MODEL WITH EXACT THEORY (CASE B).

Check Case C

Check Case C again considered one-dimensional transient heat conduction in a detector slab, but for this case the heat source was a constant irradiance on the top surface instead of a constant temperature boundary at the bottom surface. In this case, the detector bottom and sides were perfectly insulated and no heat loss by radiation or convection was allowed.

Carslaw and Jaeger also give the exact solution for this problem when the initial temperature is zero [11]:

$$T(z,t) = \frac{E_o t}{CL} + \frac{E_o L}{K} \left\{ \left(\frac{3z^2 - L^2}{6L^2} \right) - \frac{2}{\pi^2} \sum_{n=1}^{\infty} \left[\frac{(-1)^n}{n^2} \exp\left(-\frac{Kn^2 \pi^2 t}{L^2}\right) \cdot \cos\left(\frac{n\pi z}{L}\right) \right] \right\} \quad (79)$$

Very good comparisons between the analytic and code temperatures resulted from the code run described below.

In this Run C, a detector of typical dimensions (see Table 1) was divided into ten horizontal layers, and was surrounded by materials with zero thermal conductivity to obtain perfect insulation. The detector was again heated by a 0.05 w/m^2 irradiation for 1 ms in $10 \mu\text{s}$, time steps. The calculated temperatures for the layers agreed well with the theoretical temperatures (see Figure 9).

Check Case D

Check Case D, like Check Case C, considered the one-dimensional transient heat conduction in a detector slab heated by a constant irradiance on the top surface. Again the sides were perfectly insulated, but unlike Check Case C, the bottom surface was a constant temperature boundary rather than an insulated one.

Carslaw and Jaeger [11] again give the exact solution for this problem when the initial detector temperatures and the constant boundary temperature are zero:

TABLE 1. CHECK CASES A THROUGH J.

CASE	CONFIGURATION	IRRADIANCE (W/M ²)	CHOPPING RATE (Hz)	DETECTOR DIMENSIONS (M)			GENERAL DESCRIPTION OF BOUNDARY CONDITIONS
				LENGTH	WIDTH	THICKNESS	
A	SINGLE DETECTOR	0.05	NONE	101.6E-6	101.6E-6	50.E-6	HEAT GAINED BY THERMALLY LUMPED, INSULATED DETECTOR DUE TO CONSTANT IRRADIANCE; NO RADIATIVE HEAT LOSS
B	SINGLE DETECTOR	NONE	NONE	101.6E-6	101.6E-6	50.E-6	HEAT GAINED BY CONDUCTANCE THROUGH BOTTOM; NO HEAT LOSS
C	SINGLE DETECTOR	0.05	NONE	101.6E-6	101.6E-6	50.E-6	HEAT GAINED BY CONSTANT IRRADIANCE; NO HEAT LOSS
D	SINGLE DETECTOR	0.05	NONE	101.6E-6	101.6E-6	50.E-6	HEAT GAINED BY CONSTANT IRRADIANCE; HEAT LOST ONLY THROUGH CONDUCTION TO CONSTANT TEMPERATURE BASE
E	SINGLE DETECTOR	0.05	NONE	12.5E-3	25.E-6	5.E-6	HEATED BY SPATIAL STEP IRRADIANCE; HEAT LOSS BY CONDUCTION THROUGH BOTTOM AND BY EMISSION OF RADIATION (OR CONVECTION) AT TOP
F	SINGLE DETECTOR	0.05	NONE	12.5E-3	25.E-6	5.E-6	HEATED BY SPATIAL SINUSOID IRRADIANCE; HEAT LOSS BY CONDUCTION THROUGH BOTTOM AND BY EMISSION OF RADIATION AT TOP
G	SINGLE DETECTOR	0.05	NONE	12.5E-3	25.E-6	5.E-6	HEATED BY SPATIAL SINUSOID IRRADIANCE; HEAT LOSS BY CONDUCTION THROUGH BOTTOM AND BY EMISSION OF RADIATION AT TOP
H	APPROXIMATE CIRCULAR ARRAY	0.05	NONE	25.4E-6	25.4E-6	12.7E-6	HEATED BY IMPULSE IRRADIANCE; HEAT LOSS BY THREE-DIMENSION CONDUCTION AND BY CONVECTION AND EMISSION OF RADIATION AT TOP
I	LINEAR ARRAY	0.025-75.0	50-500	25.4E-6 TO 50.E-6	25.4E-6 TO 50.E-6	6.E-6 TO 25.E-6	HEATED BY CHOPPED LINE IRRADIANCE; HEAT LOSS BY CONDUCTION DOWNWARD AND ALONG ARRAY DIRECTION AND BY EMISSION OF RADIATION AND CONVECTION AT TOP
J	CRUCIFORM ARRAY	0.05	NONE	25.4E-6	25.4E-6	12.7E-6	HEATED BY IMPULSE IRRADIANCE AT CENTER; HEAT LOSS BY CONDUCTION DOWNWARD AND EMISSION OF RADIATION AND CONVECTION AT DETECTOR TOP AND SIDES

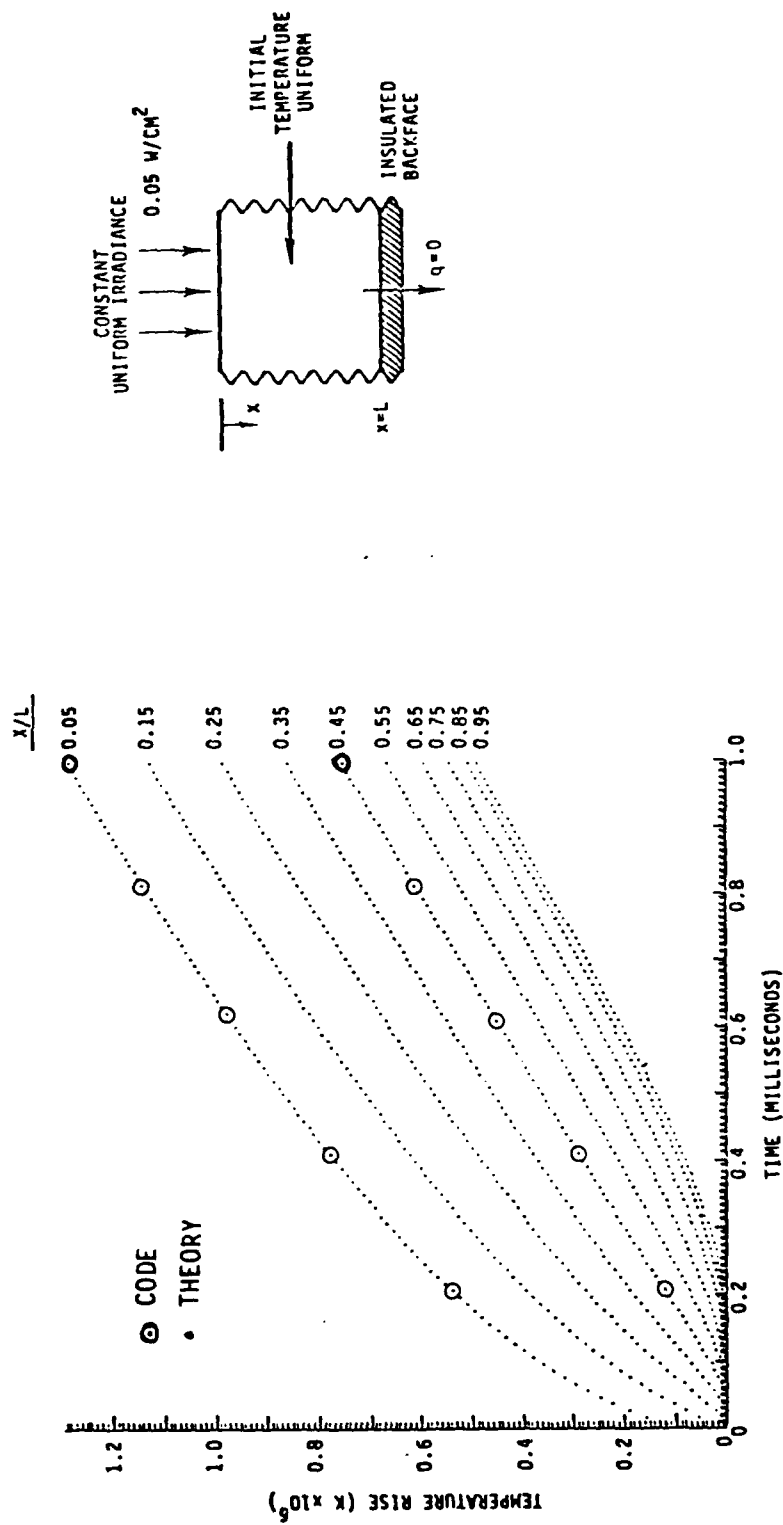


FIGURE 9. COMPARISON OF THERMAL FOCAL PLANE ARRAY MODEL WITH EXACT THEORY (CASE C).

$$T(z, t) = \frac{E_o z}{K}$$

$$- \frac{8E_o L}{K\pi^2} \sum_{n=0}^{\infty} \left\{ \frac{(-1)^n}{(2n+1)^2} \exp \left[- (2n+1)^2 \left(\frac{\pi^2}{4} \right) \left(\frac{Kt}{L^2} \right) \right] \cdot \sin \left[(2n+1) \left(\frac{\pi}{2} \right) \left(\frac{z}{L} \right) \right] \right\}$$

(80)

Again, very good agreement between analytic and calculated temperatures resulted from the code run described below.

In Code Run D, the detector and pedestal were given identical dimensions and thermal properties and divided into ten layers each so that a detector slab with 20 layers was modeled, as in Case B. The initially isothermal detector was set upon a boundary whose temperature remained constant at the detector's initial value. The detector was surrounded by perfect insulation and heated by a constant 0.05 w/m² irradiance. The resulting layer temperatures agreed well with those predicted by theory (see Figure 10).

CHECK CASES E THROUGH J

The code validation process continued with Check Cases E through J where the heating of detector material was caused by a modulated irradiance. Check Cases E through G compared code predicted and theoretical temperatures, resulting from a spatially modulated irradiance, in long, thin slabs. Check Case H studied an approximately circular detector array with an impulse irradiance on its center. Check Case I considered a linear detector array irradiated with a temporally chopped line source. The temperature information from this case was used to determine thermal responsivities and crosstalk. Check Case J studied a cruciform detector array that had an impulse irradiance on its center and had no insulation material between detectors. A more detailed description of these check cases follows.

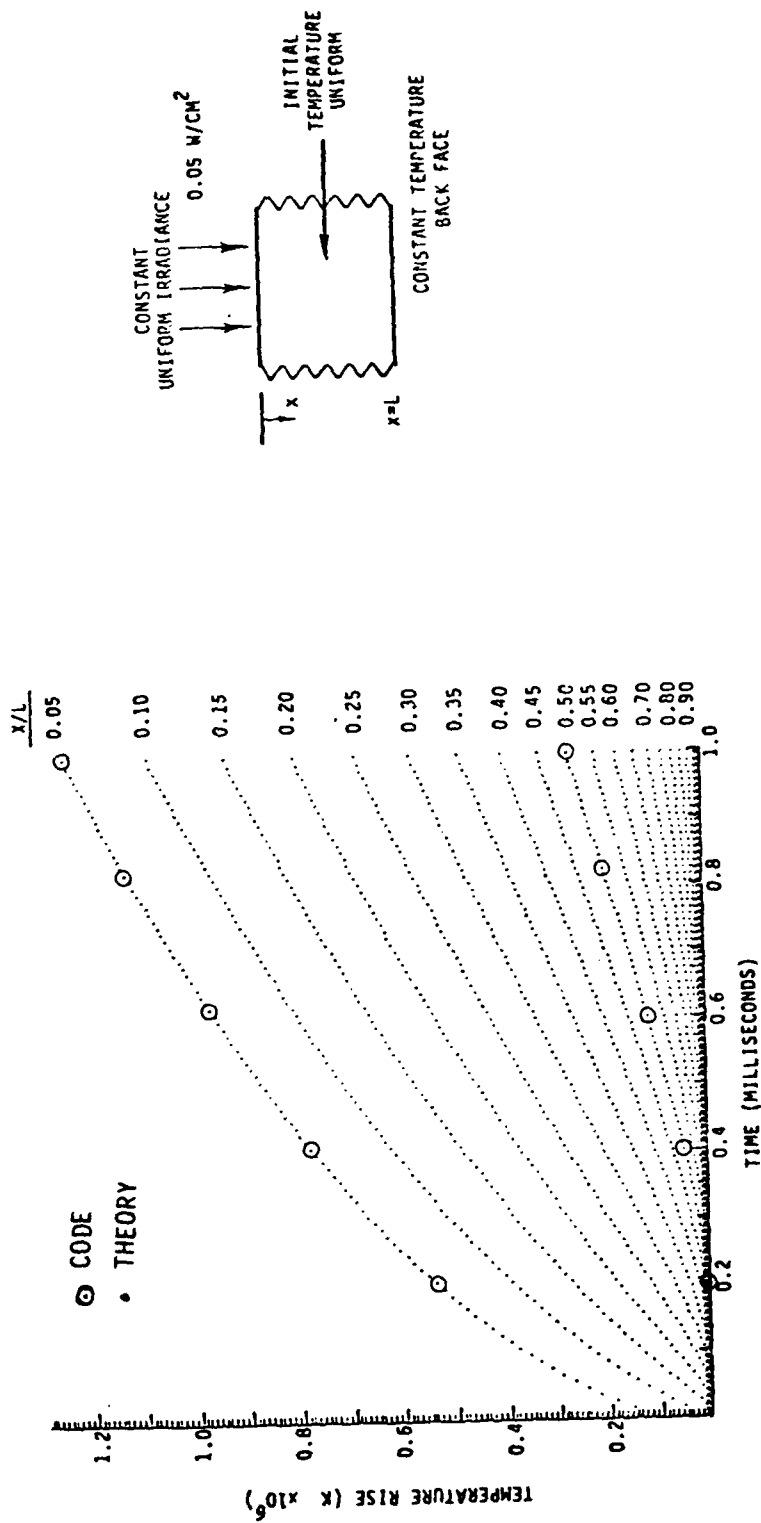


FIGURE 10. COMPARISON OF THERMAL FOCAL PLANE ARRAY MODEL WITH EXACT THEORY (CASE D).

Check Case E

This test case modeled a long, thin, perfectly insulated detector heated by an irradiance which was spatially modulated as a periodic step function. Emission of radiation eventually allowed the detector to approach thermal equilibrium. The temperatures along the detector in near thermal equilibrium as predicted by the code were compared to the temperatures derived analytically. The analytic expression for temperature difference between the detectors and the ambient, ΔT , as a function of position, x , at thermal equilibrium is given as [4]

$$\Delta T(x) = A \left[1 + \sum_{m=0}^{\infty} B_m \sin \frac{(2m+1) \pi x}{S} \right] \quad (81)$$

where: $A = E_0 / 4\sigma T_0^3$

$$B_m = \frac{4}{\pi(2m+1)} \left[\frac{1}{1 + \frac{k d (2m+1)^2 \pi^2}{4\epsilon \sigma T_0^3 S^2}} \right]$$

T_0 = Initial temperature and temperature to which heated detector emits radiation (Kelvin)

k = Thermal conductivity (joules/sec/K/m)

d = Detector thickness (meters)

S = Length of irradiation step (meters)

This expression assumed that the irradiance is off in the region where $-S < x < 0$ and on where $0 < x < S$, and periodic every length of $2S$. This expression showed that the temperature at equilibrium was periodic every $2S$, and that no significant temperature gradients exist at $x = \pm S/2$. Thus the code used a detector with perfect insulation at $x = \pm S/2$ to model an infinitely long detector under a periodic step irradiance. Six different runs were made for Test Case E and are described below. Run E-5 gave temperatures that agreed extremely well with the analytic temperatures.

Run E-1

The code used a 2.5 mm long and 5 μm thick detector divided into 20 x-direction nodes that are initially at ambient temperatures. Half of the detector was irradiated with 0.05 w/m^2 for 10,000 time steps of 45 μs duration each. At the end of the run, thermal equilibrium had not yet been attained; more time steps were needed. The node temperatures did show, however, that the theoretical distribution from the analytic expression had begun to form (see Figure 11).

Run E-2

In this second code run, the analytic temperatures at equilibrium were inserted as the code's initial temperatures to check that the code did not change them during the run. In 1,000 time steps, the temperatures had been changed negligibly with the exception of the temperatures of the nodes on either side of the on/off boundary.

Run E-3

From Run E-1 it seemed impractical to run the code until the node temperatures increased from ambient to equilibrium. The calculational time step of 45 μs was at the ceiling of allowable increments for guaranteed stable solutions, (see Section 4.1) but a larger time increment would allow for a faster approach to equilibrium if an instability would not cause a problem. These new runs found stable solutions for 4.5 ms increments but unstable for increments of 1.0 seconds or greater.

Run E-4

Node temperatures successfully increased from ambient to their respective equilibrium temperatures in only 1,000 time steps when 45 ms steps were used. These equilibrium temperatures agreed quite well with the analytic temperatures, except at nodes at the on/off boundary, where slight differences occurred (see Figure 12).

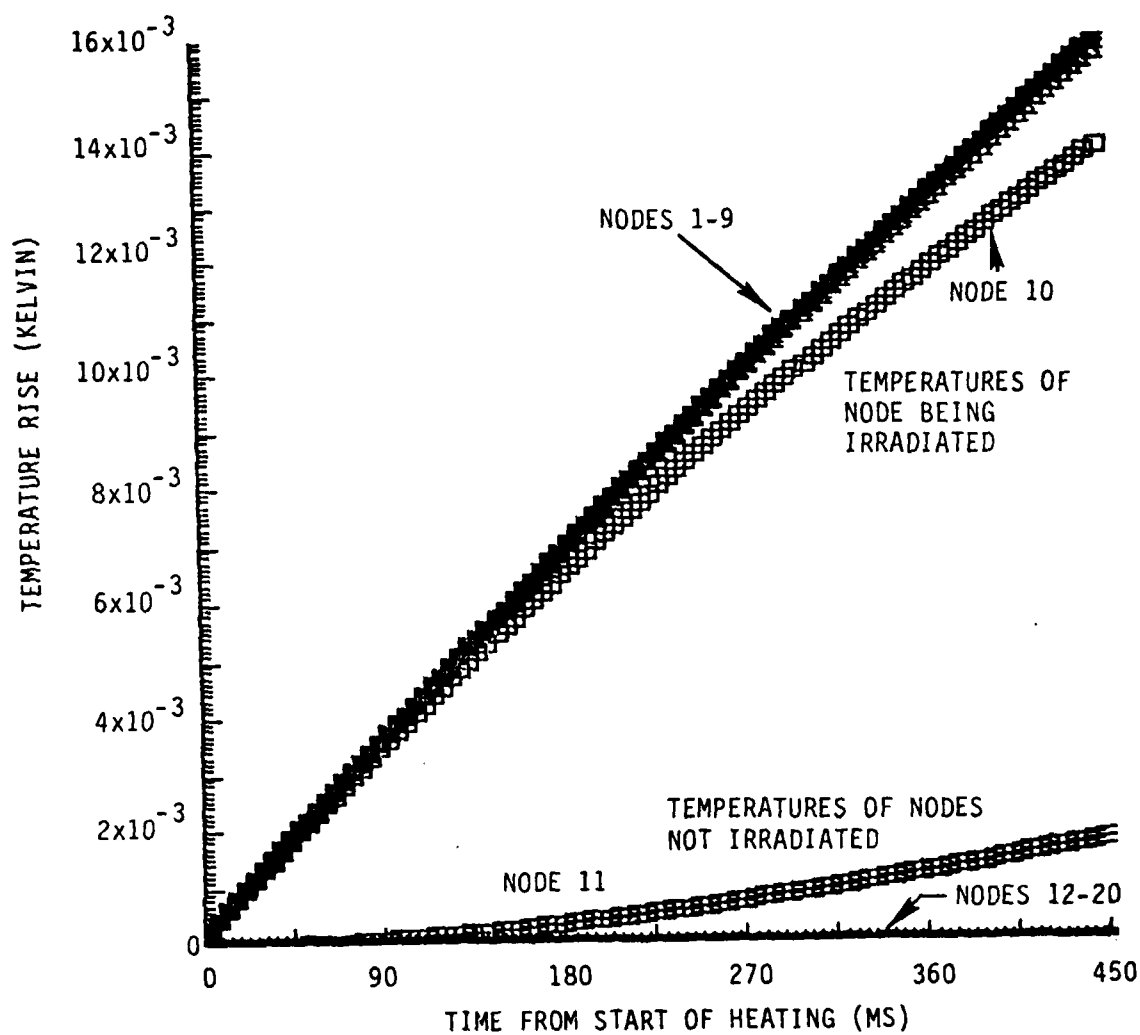


FIGURE 11. CODE RESULTS FOR CHECK CASE E, SHOWING THE BEGINNING OF THE FORMATION OF THE THEORETICAL DISTRIBUTION, RUN E-1.

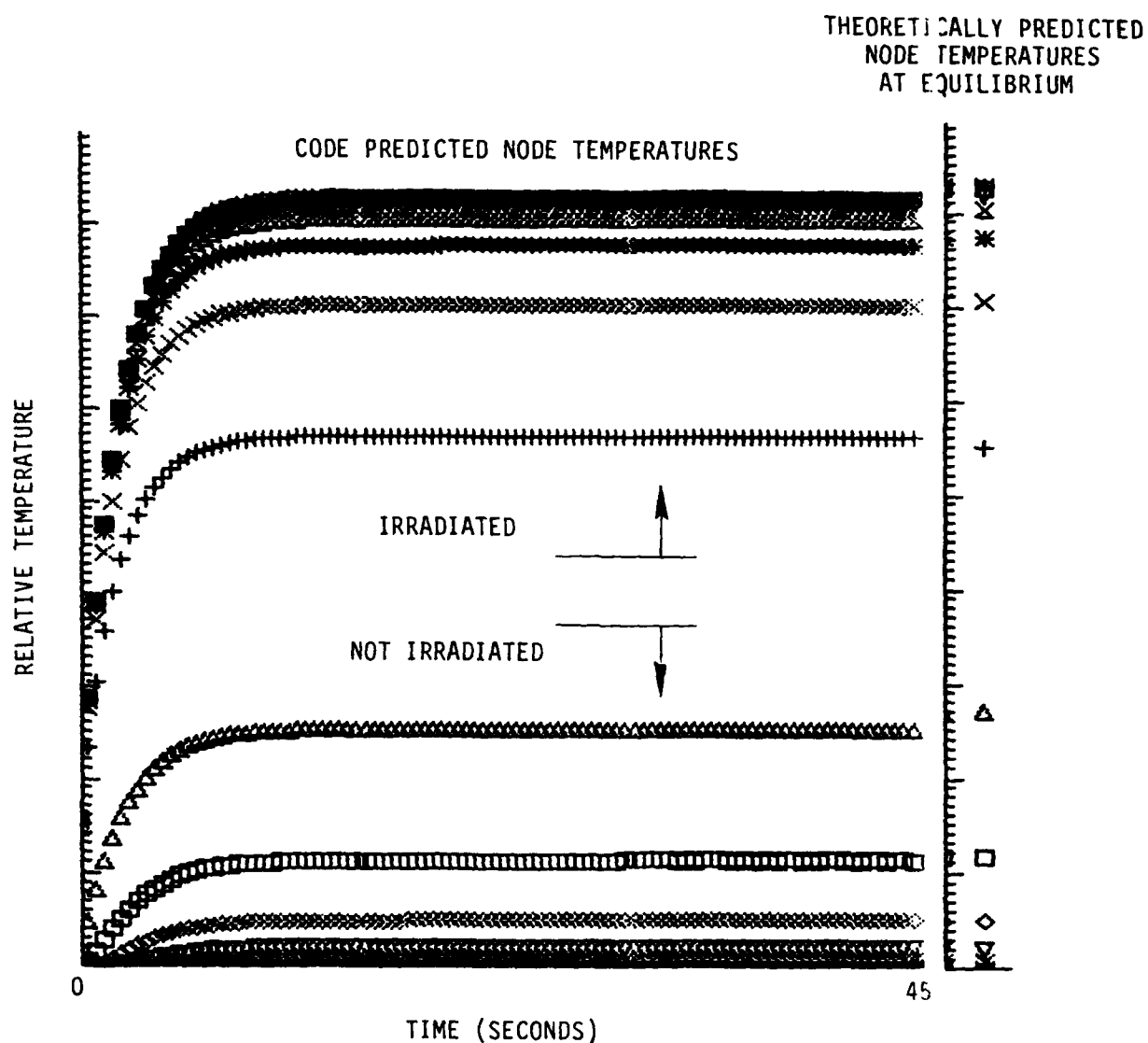


FIGURE 12. COMPARISON OF EQUILIBRIUM TEMPERATURES FOR HALF-IRRADIATED SLAB FROM CHECK CASE E, RUN E-4, AND FROM THEORY.

Run E-5

This run used a 12.5 mm long and 5 μm thick detector divided into 60 x-direction nodes initially at ambient temperature. Again, half of the detector was irradiated with 0.05 w/m^2 for 1,000 time steps of 45 ms duration.

The equilibrium temperatures were approached more quickly in this run with more nodes, and the temperatures agreed extremely well with those from the analytic expression (see Figure 13).

Run E-6

The previous runs used a detector model whose only means of losing heat was through emission of radiation. In order to check the code's ability to transfer heat by convection, an equivalent convection coefficient was used to replace the emissive heat loss mechanism. Thus the emissivity was set to zero and the convection coefficient was chosen to give identical theoretical equilibrium temperature as before, using the same detector with 20 nodes.

Again, the 1,000 45.0 ms time steps were not sufficient to allow the node temperatures to equilibrate. Since radiation and convection are dependent on different powers of temperature, the rate at which the two heat loss mechanisms equilibrate differ (the convective power of one being slower than the radiative power of four). (Later versions of the code use convective heating proportional to temperature difference raised to the $5/4$ power.) The temperatures from this convective loss run did, however, begin to show the same theoretical temperature distribution as the radiative loss run showed (see Figure 14).

Check Case F

This test case was very similar to Run E in that it modeled a long, thin, perfectly insulated detector heated by a spatially modulated irradiance. In this case, however, the spatial modulation was a sinusoid function rather than a step function. This case, too, allowed heat to be lost by the detector through emission, so that thermal equilibrium eventually resulted after heating for some time period.

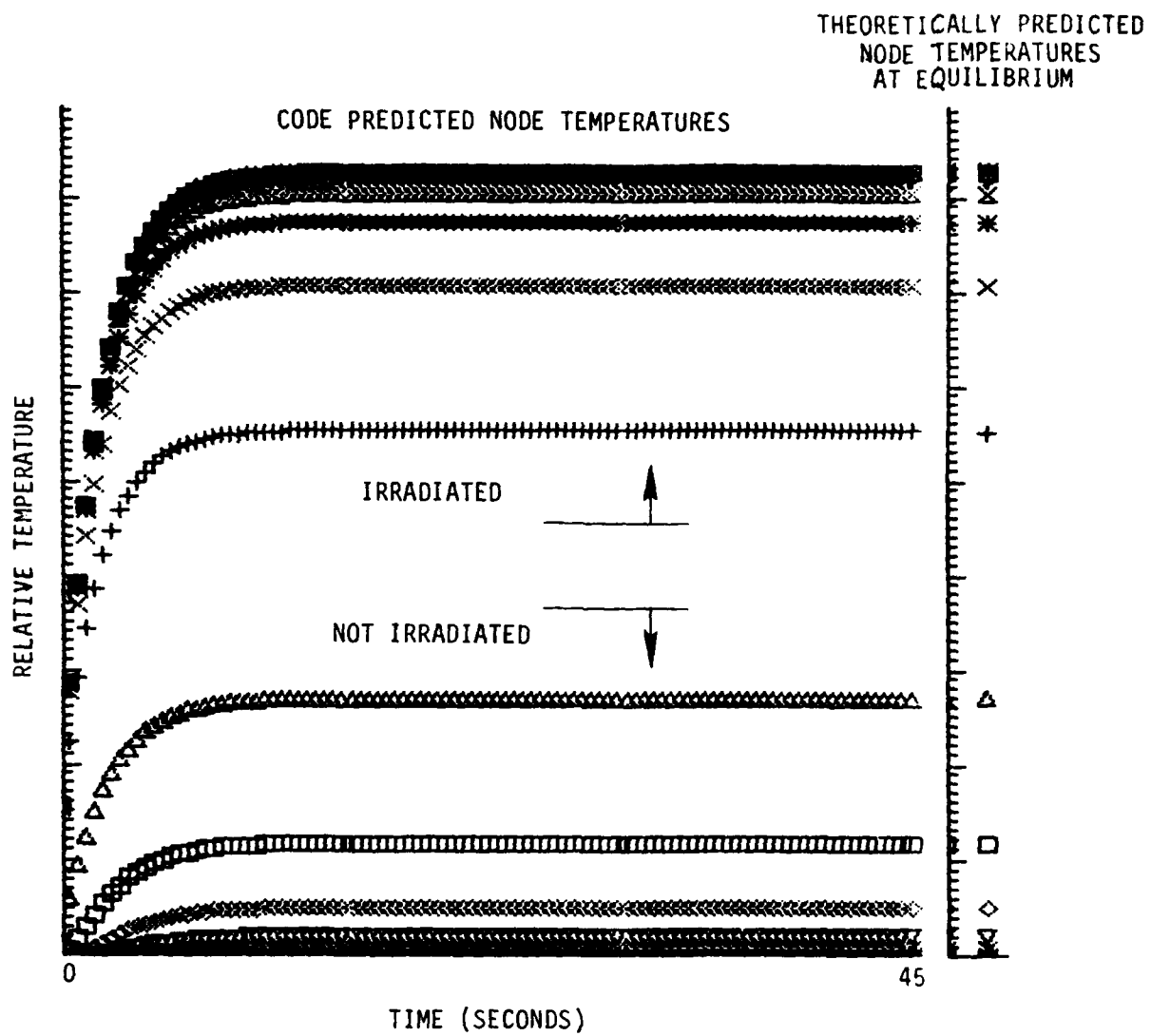


FIGURE 13. COMPARISON OF EQUILIBRIUM TEMPERATURES FOR HALF-IRRADIATED SLAB FROM CHECK CASE E, RUN E-5, AND FROM THEORY.

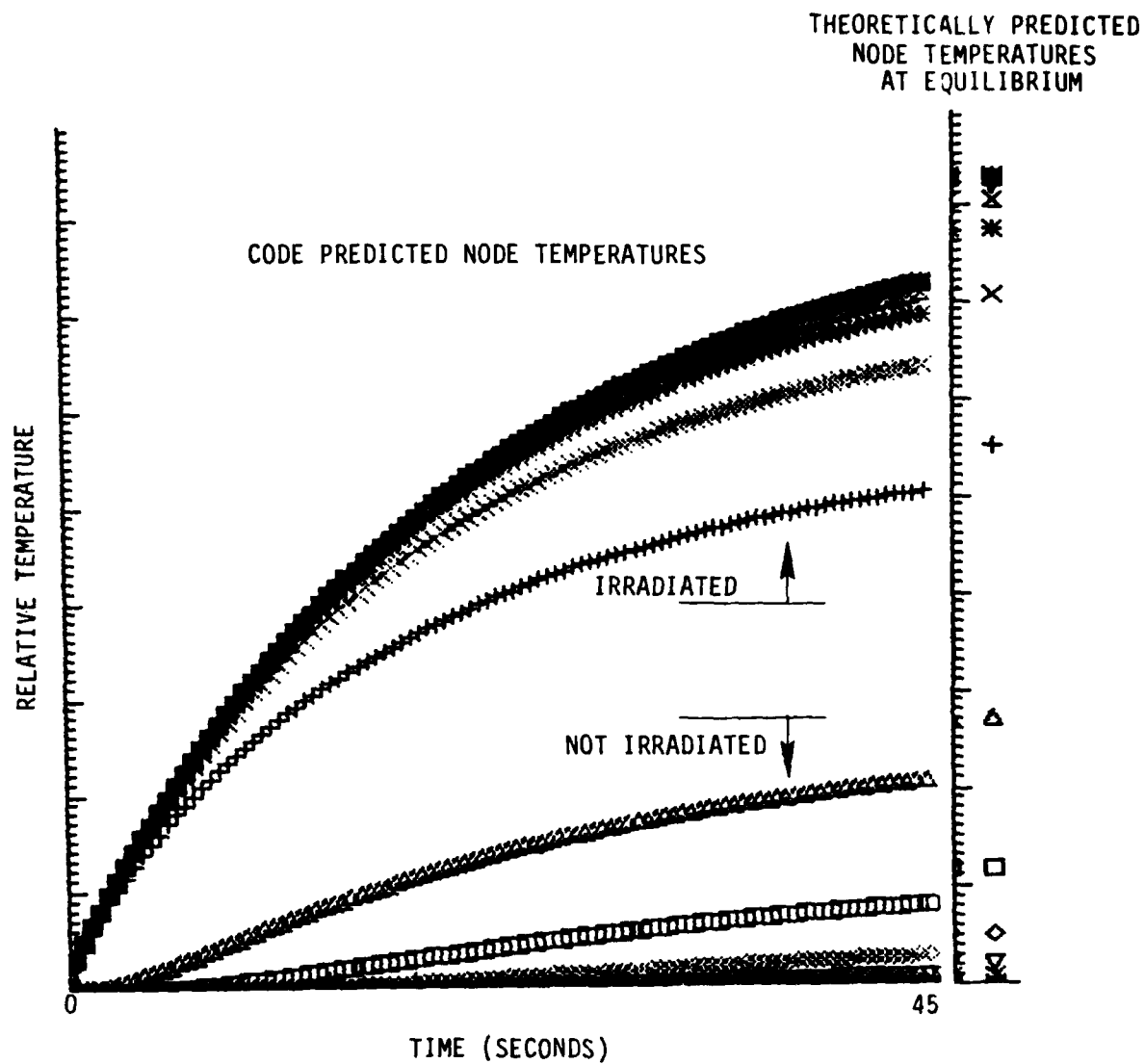


FIGURE 14. COMPARISON OF TEMPERATURES FOR HALF-IRRADIATED SLAB LOSING HEAT BY CONVECTION. CHECK CASE E, RUN E-6, AND FROM THEORY FOR THE EQUILIBRIUM CASE. EQUILIBRIUM NOT REACHED.

These equilibrium temperatures along the detector were compared to the theoretically predicted temperatures expressed analytically as:

$$\Delta T(x) = A \{1 + B \sin [(2\pi nx + \pi/2)]\} \quad (82)$$

where: $A = \frac{E_o}{4\sigma T_o^3}$

$$B = \frac{1}{1 + \frac{n^2 \pi^2 k d}{\epsilon \sigma T_o^3}}$$

T_o = Ambient temperature (Kelvin)

n = Spatial frequency (cycles/meter)

d = Detector thickness (meters)

This expression shows that the temperatures are periodic every $1/n$ distance and that no appreciable temperature gradients exist at $x=0$ and $x=1/n$. Thus, the code used a detector with perfect insulation at $x=0$ and $x=1/n$ to model an infinitely long detector under a spatially sinusoidal irradiance.

Four runs were performed for Check Case F as described below. Run F-3 gave temperatures at equilibrium that agreed very well with the analytic temperature.

Run F-1

The run used a 12.5 mm long by 5 μ m thick detector divided into 20 nodes along its length. Starting at ambient temperature, the nodes were heated under an irradiance which varied sinusoidally along the detector's length from zero to 0.1 w/m² at a frequency of 80 cycles/meter. The heating occurred for 10,000 45 μ s time steps.

As in Run E-1, not enough time was used for the nodes to reach thermal equilibrium, but the temperatures were tending toward the analytically expected distribution.

Run F-2

As in Run E-2, the theoretically predicted node temperatures at equilibrium were inserted into the code's initial temperatures to determine if the code would change them. In 5,000 45 μ s time steps, no significant changes were made, implying that the code agreed with the equilibrium temperatures.

Run F-3

It was found in Run E-5 that a calculational time increment which could have given an unstable solution actually gave stable results. So, this run also used 1,000 45 ms time steps to attempt the heating of the detector from ambient to equilibrium temperatures. The 5 μ m thick detector was divided into 60 nodes along its 12.5 mm length and was heated by 80 cycles/meter irradiance that varied from 0.0 w/m² to 0.1 w/m². This run allowed thermal equilibrium to be reached and the node temperatures agreed very well with those predicted by theory (see Figure 15).

Run F-4

This run was identical to the previous run except that transverse conduction was allowed through a common electrode instead of through the detector. The product of the thermal conductivity and thickness for the electrode in this run was identical to the product for the detector in the last run, so that identical temperatures for the two runs resulted.

Check Case G

Test Cases F and G differ only by the frequency of their spatially sinusoidal irradiances. Test Case G modeled a thin, perfectly insulated, infinitely long detector heated by an irradiance which varied sinusoidally over the detector's length. Upon heating, the detector radiation increased and eventually the detector approached thermal equilibrium where the rate of emission equaled the rate of absorption. The temperature along the detector at thermal equilibrium was predicted theoretically by the relation found under Case F, which serves as a basis of comparison for this code check case also.

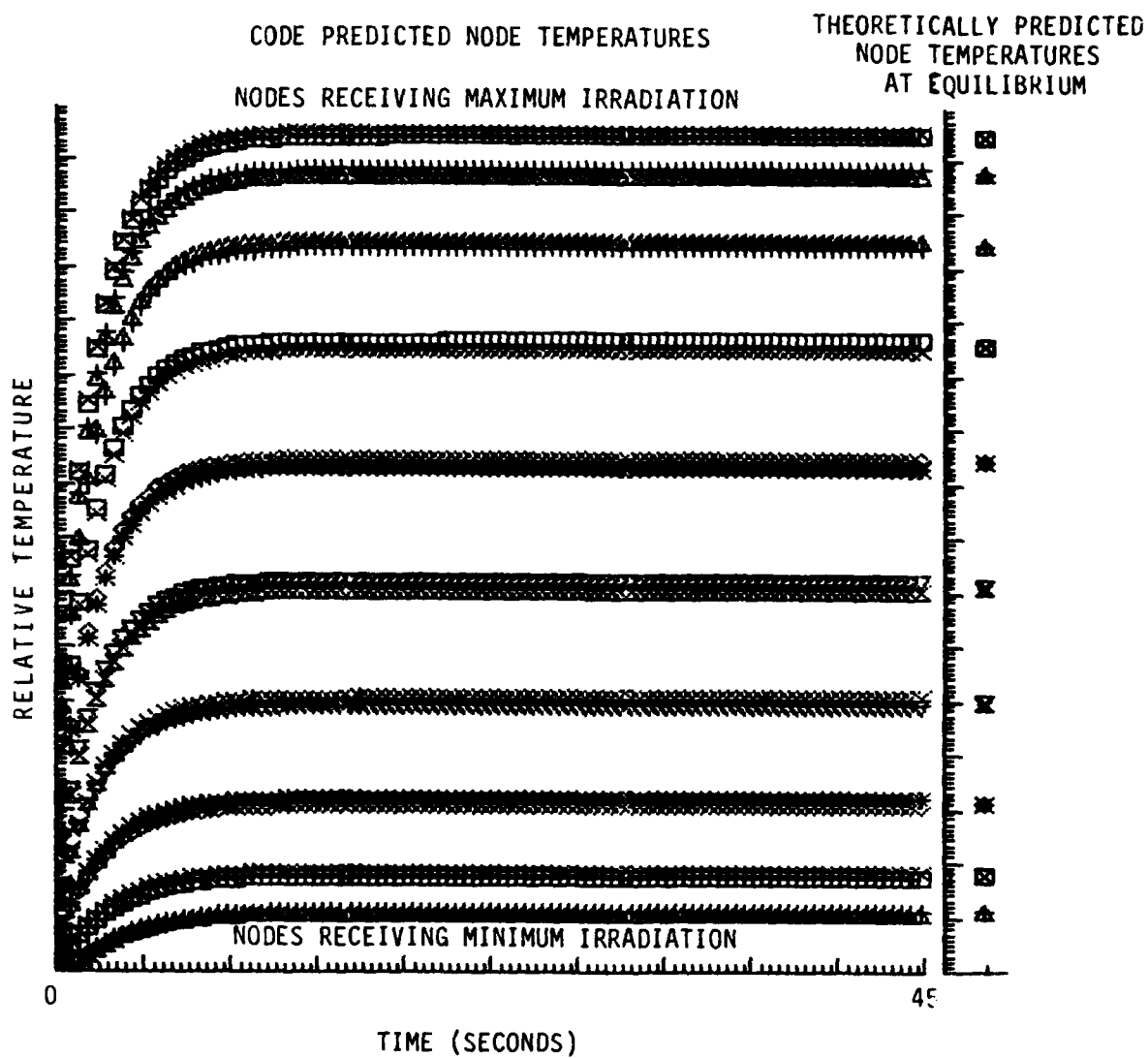


FIGURE 15. COMPARISON OF EQUILIBRIUM TEMPERATURES FOR DETECTOR SLAB IRRADIATED SINUSOIDALLY ALONG ITS LENGTH FROM CHECK CASE F, RUN F-3, AND FROM THEORY.

The following run gave equilibrium temperatures in agreement with the analytically produced temperatures.

Run G-1

A 5 μm thick detector was divided into 40 nodes along its 12.5 mm length and was initially set at ambient temperature. The detector was heated by a spatially sinusoidal irradiance which varied between zero and 0.1 w/m^2 at a frequency of 800 cycles/meter. The heating lasted for 1,000 45 ms time steps.

The node temperatures in this run successfully approached equilibrium and were in agreement with those temperatures predicted analytically.

Check Case H

Test Case H modeled a small, approximately circular, array of detectors receiving a short impulse of irradiance at the center of the center detector (see Figure 16). It was anticipated that the array would transfer the heat radially with the effective temperatures of the detectors being symmetric about any axis that passed through the center of the array. This run showed that the code handled this situation properly.

A small, roughly circular, detector array was formed from 37 detectors and briefly irradiated at the center. The square detectors were 0.001 inches on a side, divided into 25 nodes, and set on square pedestals with nine nodes. Typical thermal properties were used for the detectors, pedestals, and insulations. The irradiance was a 10 μs impulse of 0.05 w/m^2 on the center node of the array. The code gave perfectly symmetric temperature distributions for all time steps as was anticipated.

Check Case I

In Test Case I, one detector in a linear detector array received square wave chopped irradiation. The chopping effect caused the effective temperature of the detectors to fluctuate between high and low fixed values when cyclic equilibrium was reached. The difference between these high and low temperatures, the effective temperature fluctuation, gave a means for measuring

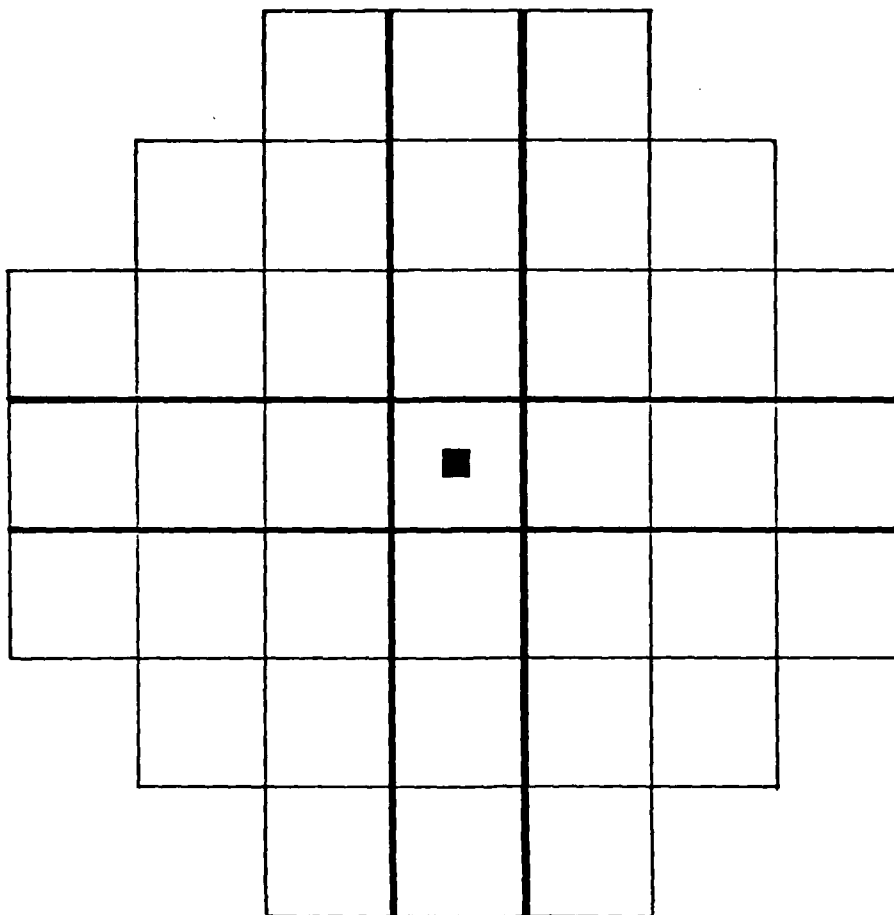


FIGURE 16. DETECTOR ARRAY MODELED IN TEST CASE H.

the thermal responsivity of the irradiated detector and thermal crosstalk between the irradiated detector and any other detector.

The test runs for this case were first used to validate and optimize the method of modeling a linear detector array. Later runs were used to simulate the effects of varying detector parameters and irradiances on the effective temperature fluctuations. A description of the test runs follows.

Run I-1

The first run was used simply to verify that the code's linear array responded to a chopped source. Twenty detectors, divided into five nodes along

their lengths, were placed into the array. The detectors had typical TGS thermal properties (see Appendix A), and were insulated and supported on pedestals. An irradiance of 0.05 w/m^2 fell on the first detector at a frequency of about 500 Hz. The effective detector temperatures that resulted did fluctuate as anticipated and the first few detectors reached cyclic equilibrium in about ten chop cycles.

Run I-2

For this run the chopped source narrowed to only one node width and the irradiated detector was at the center of a 19 detector linear array, and the chop frequency was reduced to around 50 Hz. The resulting effective temperatures were symmetric as anticipated, but the computational time was excessive. This run required approximately 13 hours on our DEC VAX 11/730.

Run I-3

The previous run gave duplicate effective temperatures on either side of its center of symmetry and thus wasted computational time. In order to consider only one-half of the array, however, the detectors had to be divided into an even number of nodes, with the two center nodes being irradiated on the center detector. This gave an integral number of nodes on either side of the array's center of symmetry. The run here described served as a check for a later run and was similar to the last run in all respects except that there were six detector nodes, two nodes being irradiated on the center detector. It too gave symmetric effective temperatures around its center of symmetry and used excessive calculational time.

Run I-4

This series of runs first checked the code's ability to work with only one-half of a symmetrically irradiated linear array and then studied the effect of varying irradiance levels on the effective temperatures. Only ten of the 19 detectors of the previous run were used, but all other array properties were unchanged for the first trial run.

The ten detectors for the first trial run behaved identically to their counterparts in Run I-3. Thus much less computational time was required for a symmetric case. The other trial runs in this group showed that the effective temperature fluctuation at cyclic equilibrium was proportional to the irradiance over a wide range of values. From a low irradiance value of 0.025 w/m^2 to a value of 75 w/m^2 (corresponding to an $8\text{-}12 \mu\text{m}$ radiation from a target whose temperature exceeds the detector temperature by about 100K), the effective temperature variation was linear with irradiance.

Run I-5

In this series of trial runs, linear detector arrays consisting of different materials were irradiated at different chopping frequencies in order to study the effects on the thermal responsivity and the thermal crosstalk between detectors. The results were then compared to similar results generated by a HEOD model [8]. A detailed description of results from these runs and the comparisons is found in Section 7.

Run I-6

This series of runs checked to see how the width of the "delta function" of irradiation on a detector in a linear array affected the thermal responsivity and the thermal crosstalk. It was found that narrowing the irradiation strip from one-third to one-sixth of the detector width resulted in negligible changes in detector responsivity and crosstalk. Widening the strip to include all of the detector surface, however, resulted in more crosstalk and significantly increased responsivities.

Check Case J

This test case modeled a five detector cruciform array with no solid insulation between detectors. This array was given a short irradiation pulse at the center node to determine if the effective temperatures remained symmetric about the center. Unlike previous cases where heat was conducted between detectors through insulation, the heat transfer between detectors in this case was by radiation. Also in this case, heat loss by convection from surfaces previously contacted by insulation was included. The following description of trial runs describe how the model performed.

Run J-1

This trial run sent a 20 μs pulse of a 0.05 w/m^2 irradiation to the center of a cruciform array. The array consisted of five $25.4 \mu\text{m}$ square detectors separated by $2.54 \mu\text{m}$. The center detector was heated and lost heat properly through convection and conduction, but did not transfer any appreciable radiation to adjacent detectors (i.e., less than $10\text{E}-38 \text{ w}$, the limit of the computer). According to this model, the detector's temperature must be significantly higher before appreciable emissive losses occur.

SECTION 7. EVALUATION OF TYPICAL THERMAL FOCAL PLANE ARRAYS

The TFPA code was used to model several linear arrays and materials being considered by the community. The materials chosen for study consisted of LiTaO_3 , PVF_2 , DTGFB and BaTiO_3 , which are representative of work currently being pursued in industry [12]. A quantitative description of the arrays is given below followed by a discussion of the responsivities and crosstalks predicted.

LiTaO_3 , PVF_2 and DTGFB Detector Arrays

The LiTaO_3 , PVF_2 and DTGFB arrays consisted of thin sheets of pyroelectric materials sectioned into 50 μm square detectors. The detector thickness, 25 μm for LiTaO_3 and DTGFB and 6 μm for PVF_2 , was uniform over the detector area except for a one-half thickness notch on the 5 μm border of the DTGFB detectors. Each detector contacted the electrode beneath it by means of an epoxy pedestal which was about two-thirds of the detector area. The LiTaO_3 array was surrounded by air, while the other arrays were evacuated.

Each linear array, built with a central detector and nine more on either side, was irradiated at the center by an approximate line source of $3.4 \times 10^{-5} \text{ w/m}^2$. This irradiance represents a target in the 8-12 μm spectral band, which is 10K warmer than ambient (taken to be 298K). The irradiance was chopped at 50, 100, 200 and 400 Hz in order to study the thermal responsivity of the center detector and the thermal crosstalk between the first, second, third and fourth detectors.

The code was usually instructed to divide the individual detectors into eight nodes in the direction of the array; two 5 μm nodes at the borders and six nodes for the remaining 40 μm length. In the direction perpendicular to the line array, only three nodes were used; two were 5 μm wide at the boundary and one was 40 μm in width. For each frequency studied, the code operated for two and one-half chop cycles, except for the 400 Hz case which ran for four and one-half chop cycles. Irradiation during the "on" half period was incident on only the two centermost nodes of the central detector.

BaTiO₃ Detector Arrays

The BaTiO₃ arrays used in this evaluation consisted of distinct 25 μm square detectors that were 12.7 μm thick. Each detector was positioned on an epoxy pedestal which was also 12.7 μm thick, but had only two-thirds of the detector area in contact. The detectors were separated by 0.5 μm and a glass-like insulation filled the gap between each detector pedestal assembly.

This BaTiO₃ array, built with a central detector and four more on either side, was irradiated at the center by an approximate line source of $2.16 \times 10^{-5} \text{ w/m}^2$, identical to the irradiance on the previous three arrays. This irradiance was chopped at 50, 100, 200 and 400 Hz to again study the thermal responsivities and crosstalk.

The code divided the detectors into nodes in a slightly different manner for the BaTiO₃ array. In the direction of the linear array, six nodes made up the detector length of 25 μm and a 2.5 μm insulation node was added on either side. Perpendicular to the array, one node filled the 25 μm detector width and a 5 μm insulation node was added on either side. The detector and epoxy pedestal each contained one node vertically. Five detectors were used by the code to model the nine detectors in the symmetric array. Only the two centermost nodes of the modeled central detector received the chopped irradiation, and this occurred for only 2-1/2, or 4-1/2 for the 400 Hz case, chop cycles.

RESPONSIVITY AND CROSSTALK

The thermal responsivity and crosstalk of four linear detector arrays has been determined through the use of the TFPA code at four frequencies of chopped irradiation. These results are shown in Table 2.

The thermal responsivity is given by

$$R = \frac{\Delta T}{EA} \quad (83)$$

where ΔT (Kelvin) is the effective temperature fluctuation of the irradiated detector, or the difference in volumetric average temperature at its maximum

TABLE 2. NRC SIMULATION GENERATED THERMAL RESPONSIVITIES AND CROSS TALKS FOR TYPICAL THERMAL FOCAL PLANE ARRAYS.

MATERIAL	CHOPPING FREQUENCY (Hz)	CYCLIC TEMPERATURE DIFFERENCE (K)	RESPONSIVITY (°K/W)	CROSS TALK (ACTUAL/[APPARENT]) [*] (%)		
				DETECTOR #2	DETECTOR #3	DETECTOR #4
LiTaO ₃	50	0.217E-4	7,990	54.8/[54.8]	21.6/[21.6]	10.9/[6.3]
	100	0.157E-4	5,780	42.7/[42.7]	15.7/[9.6]	4.1/[0.7]
	200	0.106E-4	3,900	24.5/[23.3]	9.1/[4.0]	5.2/[3.5]
	400	0.700E-5	2,580	22.8/[16.6]	0.0/[2.7]	0.0/[3.4]
PVF ₂	50	0.102E-3	37,540	3.9/[3.9]	0.0/[0.0]	0.0/[0.0]
	100	0.906E-4	33,350	2.0/[0.7]	0.0/[0.0]	0.0/[0.0]
	200	0.739E-4	27,200	0.4/[0.2]	0.0/[0.0]	0.0/[0.0]
	400	0.522E-4	19,210	0.0/[0.2]	0.0/[0.0]	0.0/[0.0]
DTGFB	50	0.587E-4	21,610	21.3/[21.3]	3.0/[1.0]	0.5/[0.3]
	100	0.428E-4	15,750	13.6/[9.8]	0.8/[0.6]	0.0/[0.1]
	200	0.288E-4	10,600	7.7/[3.7]	0.0/[1.1]	0.0/[0.3]
	400	0.176E-4	6,480	3.4/[1.3]	0.0/[1.2]	0.0/[0.2]
BaTiO ₃	50	0.185E-4	16,890	22.6/[24.1]	3.6/[3.8]	0.6/[0.6]
	100	0.173E-4	15,790	23.9/[23.9]	3.6/[3.6]	0.6/[0.5]
	200	0.162E-4	14,790	20.5/[20.5]	2.5/[1.6]	0.3/[0.1]
	400	0.130E-4	11,870	12.3/[11.3]	1.0/[0.6]	0.0/[0.0]

*IF ACTUAL IS LESS THAN APPARENT; CYCLIC EQUILIBRIUM WAS NOT APPARENT.

NOTE: IRRADIATED AREA = $0.533E-9 \text{ m}^2$
 $E_0 = 5.0941 \text{ W/M}^2$ (CORRESPONDING TO THE NET IRRADIANCE FROM A TARGET WHOSE TEMPERATURE IS 10 DEGREES ABOVE THE DETECTOR TEMPERATURE)

and minimum over a chop cycle, $E \text{ (w/m}^2\text{)}$ is the irradiance, $A \text{ (m}^2\text{)}$ is the irradiated area, and $R \text{ (K/w)}$ is the thermal responsivity.

Thermal crosstalk is given by

$$CT = \frac{\Delta T_n}{\Delta T} \times (100\%) \quad (n=2,3,4) \quad (84)$$

where ΔT_n (Kelvin) is the effective temperature fluctuation for detectors not irradiated, ΔT (Kelvin) is again the effective temperature fluctuation for the irradiated detector, and CT (percent) is the thermal crosstalk between the irradiated and n^{th} detectors. Table 2 includes an actual and apparent crosstalk

term. The actual crosstalk is determined from the maximum effective temperature fluctuation of a non-irradiated detector. Apparent crosstalk, however, is determined by the differences in effective temperature at the start and finish of a chop half-cycle which is not necessarily in phase with the times of maximum and minimum temperatures. (Apparent crosstalk, then, indicates the signal dispersion that a chopper-synchronized CCD would read.)

The thermal responsivity and crosstalk were found to vary as the array and irradiance varied. The following discussion reports how the effects of chopping frequency, array materials and dimensions, code variables, approximate line source widths, and irradiation levels changed responsivity and crosstalk values.

Chopping Frequency

As expected, thermal responsivity drops off as the chopping frequency increases. The calculated responsivity is not constant between 50 and 100 Hz, so an even lower chopping frequency would be needed to observe this leveling off. Thermal crosstalk decreases as the chopping frequency increases. Thus a tradeoff is shown for responsivity and spatial resolution.

Array Materials and Dimensions

The best responsivities came from the PVF_2 array. the remaining arrays ranked in decreasing order of their responsivities were the BaTiO_3 , DTGFB and LiTaO_3 arrays. A very rough relationship from the results showed that the responsivities at lower chopping frequencies were nearly proportional to the heat capacities and thicknesses of the detectors and inversely proportional to the detector thermal conductivities.

The arrays ranked in order of increasing percent thermal crosstalk are the PVF_2 , DTGFB, BaTiO_3 and LiTaO_3 . Again, a very rough relationship exists where the thermal crosstalk is nearly proportional to the thermal conductivity of the material joining adjacent detectors.

Code Variables

Neither the responsivity nor the thermal crosstalk values changed significantly when two vertical nodes were used in each of the pedestal and detector instead of one node each. Similarly, doubling the number of nodes in the linear array direction had little effect (i.e., less than 0.1 percent).

Approximate Line Source Widths

Both the responsivity and crosstalk increased when the irradiation was incident upon the entire detector surface as opposed to only about one-third of the surface. However, when irradiation was incident on only about one-sixth of the surface as opposed to about one-third, there was no significant change in either responsivity or crosstalk.

Irradiance Levels

No significant changes in responsivity were found when irradiance levels changed. The effective temperature fluctuations were found to be proportional to irradiance over a wide range of values (i.e., from 0.025 to 75.0 w/m²).

HEOD's MODELS

The LiTaO₃, PVF₂ and DTGFB detector arrays modeled by the TFPA code were based upon similar arrays used in HEOD's code [8]. The thermal responsivities generated by both codes are shown in Figure 17. It can be seen that the HEOD code yielded lower responsivities in each case, due probably to different modeling techniques. Percent crosstalk values for each code's treatment of the LiTaO₃ array is shown in Table 3. HEOD's values are slightly higher for the crosstalk to the first adjacent detector, but smaller for the second adjacent detector (32 percent smaller) and significantly smaller for the third adjacent detector (factor of about 11 percent smaller).

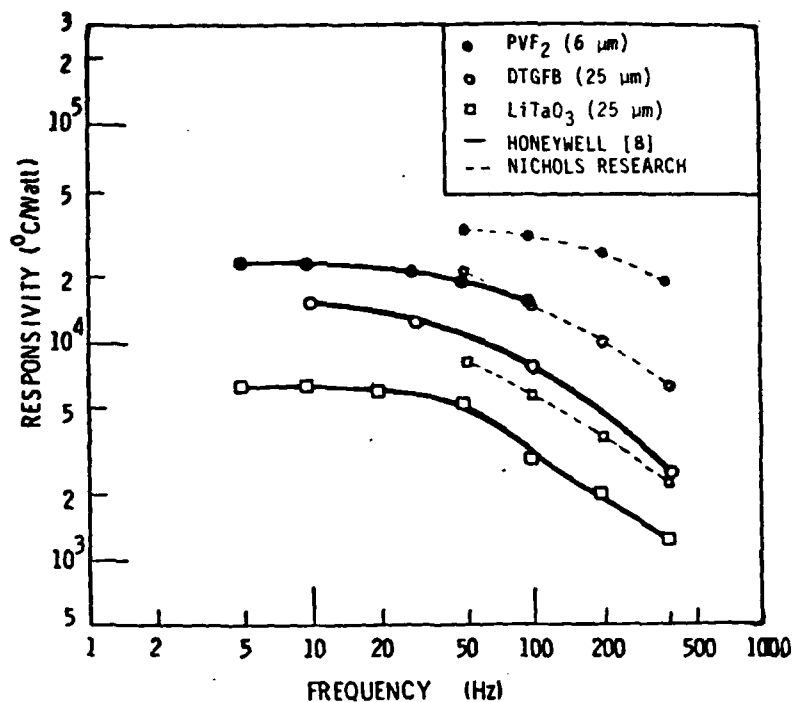


FIGURE 17. COMPARISON OF THERMAL RESPONSIVITY VERSUS CHOPPING FREQUENCY PLOTS FROM HEOD'S NODAL ANALYSIS CODE AND FROM NRC'S TFPA CODE.

TABLE 3. COMPARISON OF THERMAL CROSSTALK RESULTS FOR HEOD [8] AND PRESENT MODELS

FREQUENCY (Hz)	FIRST ADJACENT DETECTOR		
	HONEYWELL MODEL	PRESENT MODEL	
	MAXIMUM	MAXIMUM	APPARENT
50	57.5	54.8	54.8
100	41.3	42.7	42.7
200	28.1	24.5	23.3
400	24.1	22.8	16.6

MAXIMUM - CROSS TALK EVALUATED FROM MAXIMUM TEMPERATURE DIFFERENCE

APPARENT - CROSS TALK EVALUATED FROM MAXIMUM TEMPERATURE DIFFERENCE WITH READOUT SYNCHRONIZED WITH CHOPPER

SECTION 8. RESULTS

Some of the more important results of the study are summarized in this section. The accuracy of the code compared to exact analytical solutions is shown in Table 4 for some of the validation cases considered.

It is seen that the code has adequate accuracy for the purpose of relative performance evaluation of focal plane arrays. The check cases were selected to test various parts of the code under conditions comparable to laboratory or field tests.

The present thermal model predicts responsivities that are about a factor of two larger than those predicted by the HEOD's model for their assumed configuration and materials. The exact configuration and properties used by HEOD were not given in available documentation [8]. The crosstalk predicted by the present model is within about 5 percent of that predicted by the HEOD model.

TABLE 4. PERCENT ERROR IN CODE VERSUS THEORY PREDICTION AT ΔT VERSUS TIME.

$$\epsilon = \left[\frac{\Delta T_c - \Delta T_t}{\Delta T_t} \right] \times 100$$

CASE		X/L	NODE	ϵ (%)	
				600 μ s	1000 μ s
B	TOP	0.025	6	-6.4	-1.4
	MIDDLE	0.475	87	-0.13	-0.04
C	TOP	0.05	6	0.18	0.08
	MIDDLE	0.45	42	0.21	0.12
D	TOP	0.025	6	0.13	0.08
	MIDDLE	0.475	87	-0.34	-0.11

SECTION 9. CONCLUSIONS

A fully operational thermal/electrical computer model has been developed for evaluating the performance of pyroelectric thermal detectors. This model allows evaluation of rather general design configurations with adjustable dimensions and properties (thermal and electrical), under arbitrary field or laboratory conditions. The computer code has been thoroughly validated against a series of exact solutions for a variety of theoretical situations. As far as was practical, the model was based on first principles formulations with reasonable simplifying conditions. The code was designed for a high degree of "user-friendliness," as well as for modularity to facilitate code understanding and modification.

The model was checked against the one-dimensional thermal model results published by HEOD and found to give similar results. Detector responsivity predicted by the HEOD model are about a factor or two smaller than those of the NRC model. This difference is probably due to differences in the model or input parameters. The predicted crosstalk of the two models is surprisingly close; within about five percent.

SECTION 10. RECOMMENDATIONS

This preliminary development effort provides a useful design tool, and uncovers the important phenomenology for future developments. NRC recommends that the code be exercised in a well-planned series of computer "experiments" to evaluate the effects of various design parameters on the theoretical performance of typical sensor concepts. Several code upgrades and modifications are desirable to investigate more accurately the key phenomenological effects. Specifically, NRC recommends that the following technical analysis and development tasks be completed as soon as possible.

- Task 1. Define the model input parameters to characterize several leading pyroelectric detector systems of interest (e.g., systems by TI, HEOD).
- Task 2. Design a series of computer experiments to evaluate performance sensitivity to design parameters (e.g., materials, dimensions, configuration, chop rate, readout rate, processing noise parameters). The major output of this task should be a matrix of design parameter values over which the sensitivity analysis would be run, and a set of nominal values.
- Task 3. Simulate the performance of the matrix of sensors (defined in Task 2) for an actual irradiance scene, measured by a high performance calibrated infrared imaging system filtered in two or more spectral bands (e.g., 3-5 μm and 8-12 μm). The performance sensitivity should be characterized by parameters such as MTF (thermal and electrical); thermal crosstalk to adjacent detectors and detectors two and three away from an irradiated detector; detector responsivity as a function of electrical frequency (w); NEP and NE ΔT versus w ; D^* .
- Task 4. Various implicit techniques (e.g., Crank-Nicholson) should be examined for possible application in the TFPA code. If reasonable, the code should be modified to use an implicit technique as an option, and comparisons made with the existing explicit technique.
- Task 5. The TFPA code should be modified to consider the effects of heat conduction through the bottom electrode.
- Task 6. A more accurate treatment of the radiative heat transfer between adjacent detectors should be developed.
- Task 7. Formulate necessary equations and expand code to provide the system throughput in response to the application of arbitrary stationary radiation patterns to the focal plane.

- Task 8. Formulate necessary equations and expand code to provide the system throughput in response to the application of arbitrary time-varying radiation patterns to the focal plane.
- Task 9. Investigate system MTF as a function of geometrical point of application of δ -function radiation input; perhaps devise more representative way in which to formulate system MTF.
- Task 10. Using representative system and operational parameters, investigate the limits of strict applicability of the code with respect to linearity, appropriateness of the use of MTF, etc. Investigate correlation of behavior in orthogonal directions on focal plane. A consideration of alternative system figures-of-merit which are appropriate to thermal focal planes might be useful.
- Task 11. Develop the necessary software to produce computer generated graphical output of various simulation output parameters of interest.

REFERENCES

1. B. Ball, Analysis and Modeling for Thermal Focal Plane Arrays, Computer Documentation (Internal), Nichols Research Corporation, Ann Arbor, Michigan, NRCAA-TR-84-002, 10 February 1984.
2. S. Buchbinder, Analysis and Modeling for Thermal Focal Plane Arrays, Computer Program Configuration Item Maintenance Manual (Operational Software), Nichols Research Corporation, Ann Arbor, Michigan, NRCAA-TR-84-003, 10 February 1984.
3. J. Mudar, Analysis and Modeling for Thermal Focal Plane Arrays, Annotated Bibliography, Nichols Research Corporation, Ann Arbor, Michigan, NRCAA-SP-84-001, 10 February 1984.
4. T. W. Tuer, J. Mudar and R. Freeling, Analysis and Modeling for Thermal Focal Plane Arrays, Interim Report, Nichols Research Corporation, Ann Arbor, Michigan, NRCAA-TR-83-003, 15 August 1983.
5. F. Kreith, Principles of Heat Transfer, International Textbook Company, Scranton, Pennsylvania, 1958.
6. V. S. Arpaci, Conduction Heat Transfer, Addison-Wesley, 1966.
7. C. O. Bennett and J. E. Myers, Momentum, Heat and Mass Transfer, Second Edition, McGraw-Hill Book Co., 1974.
8. R. Coda, et al., Solid State Readout for Pyroelectric Retinas, Final Technical Report for Phase I, 1 February to 31 May 1978, Honeywell Research Corporation, Lexington, Massachusetts, Report No. 7807-2, December 1978 (AD B034 307).
9. N. Butler (Honeywell Research Corporation), Private communication to J. W. Lennington (Nichols Research Corporation), November 1983.
10. A. J. Steckl (Rensselaer Polytechnic Institute), "Charge-Coupled Devices," Chapter 12 of The Infrared Handbook, edited by W. L. Wolfe and G. J. Zissis, Infrared Information and Analysis Center, Environmental Research Institute of Michigan, Ann Arbor, Michigan, 1978.
11. H. S. Carslaw and J. C. Jaeger, Conduction of Heat in Solids, Second Edition, Oxford University Press, Great Britain, 1976.
12. A. T. DePersia (NVEOL), Letter containing data and information on material properties, Transmitted to Nichols Research Corporation, Ann Arbor, Michigan, June 1983.
13. M. E. Palmer III, A Program to Compute Thermal Behavior of Optical Detectors, Univ. Maryland Report, May 1983.
14. Alan V. Oppenheim and Ronald W. Schaffer, Digital Signal Processing, Prentice Hall, 1975, pp. 99-110.

APPENDIX B. THERMAL PROPERTIES OF PEDESTAL, ELECTRODE AND SUBSTRATE MATERIALS. Numbers in brackets refer to literature survey bibliography (Reference 4) and numbers in parentheses refer to references in this report.

MATERIAL	HEAT CAPACITY (ρC) (J/CM ³ -K)	DENSITY (ρ) (G/CM ³)	THERMAL CONDUCTIVITY (K) (J/CM-S-K)
AIR	.0012 (8)	.0012 (8)	5.54×10^{-4} (8)
ALUMINUM	3.0 (8)	2.7 (8)	2.0 (8)
Al ₂ O ₃	-	-	1.8×10^{-3} [123]
BAF ₂	-	-	0.12 [123]
CaF ₂	-	-	0.12 [123]
CHROMIUM	3.2 (13)	7.16 (13)	[123] 0.87-0.94 (13)
COPPER	-	-	3.9 [123]
EPOXY	(13) 1.5-2.51 (8)	(8) 1.0-1.9 (8)	(13) 0.001-0.01 (8)
GLASS	2.1 [123]	2.6 [123]	0.01 [123]
GOLD	2.5 (13)	19.3 (13)	3.2 (13)
INDIUM	1.7 [103]	7.32 (8)	0.66 [103]
KCl	1.4 [123]	2.9 [123]	0.068 [123]
MBBA (LIQUID CRYSTAL)	1.8 [123]	1.0 [123]	1.7×10^{-3} [123]
PLATINUM	2.56 (8)	21.5 (8)	0.7 (8)
SILICON	[103] 1.6-1.66 (13)	2.33 (13)	(8) 0.9-2.0 [103]
SiO	1.64 (8)	2.2 (8)	(13) 0.010-0.014 [123]

APPENDIX C

In many radiation detection schemes utilizing a two-dimensional array of detector elements, readout of the array is accomplished using standard CCD devices. Discussions of the performance properties of these devices under a wide variety of incident image characteristics have been published by several authors (see, for example, References 8 and 10). For the operation of a pyroelectric detector array, the incident radiation must be modulated because the pyroelectric charge is generated by polarization changes, which, for small temperature differences, are proportional to the change in temperature of the pyroelectric material. In the following analysis, the Fourier transform of the voltage output of a finite pyroelectric array with CCD readout is derived. In addition to utilizing a detailed model of the CCD sampling process, the action of a chopper is explicitly treated. The general result for the Fourier transformed array voltage output as a function of electrical frequency is quite complicated. Hence, to illustrate the main features of the general result which is given in Equation 28, discussion of a simple, chopped, line source is included at the end.

The conversion by a pyroelectric detector array of a chopped, static (constant in time) irradiance input to a voltage output is assumed to be a linear, convolutionary process. As such, the output from say the $(m,n)^{th}$ detector is representable as

$$V(x_m, y_n, t) = \iiint_{-\infty}^{\infty} d\tau d\xi d\eta H(x_m - \xi, y_n - \eta, t - \tau) I(\xi, \eta) C(x_m - \xi - V_x \tau, y_n - \eta - V_y \tau) \quad (85)$$

where: $H(x, y, t) \equiv$ Pyroelectric array transfer function (including transfer inefficiencies of the readout process)

$I(x, y) \equiv$ Input irradiance on array surface

$C(x, y) \equiv$ Chopper geometry

$(x_m, y_n) \equiv$ Focal plane coordinates for $(m,n)^{th}$ detector (see Figure 1)

$(V_x, V_y) \equiv$ Focal plane coordinate components of the chopper velocity.

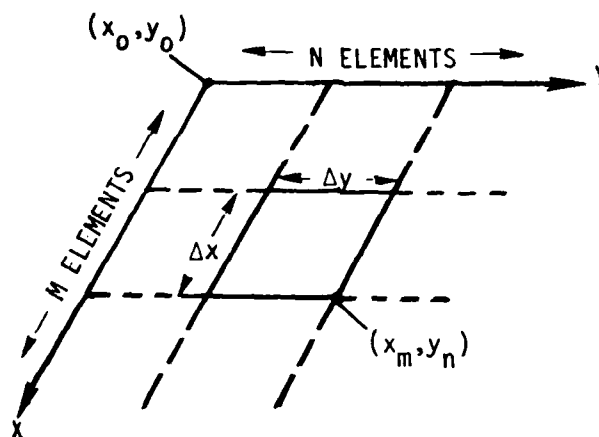


FIGURE 18. FOCAL PLANE COORDINATES FOR $(M, N)^{th}$ DETECTOR.

Equation 85 is applicable, under the stated conditions, only if the chopper contributes a negligible background compared to the image scene's irradiance. If this is not the case, the chopper contribution to the irradiance on each detector can be accounted for by writing

$$I(\xi, \eta) C(x-\xi, y-\eta) + I(\xi, \eta) C(x-\xi, y-\eta) + I_c [1 - C(x-\xi, y-\eta)] \quad (86)$$

where I_c represents the constant irradiance from the chopper. Note, only when the chopper is "closed," i.e., $C=0$, does I_c irradiate the array elements beneath the chopper. When the right hand side of Expression 86 is inserted into Equation 85 above, the term containing I_c alone contributes only to an unimportant dc or zero frequency component of the output power, hence may be dropped. The two remaining terms can be combined into an expression identical to Equation 85 with $I(\alpha\beta)$ referenced to I_c . Hence, without loss of generality, Equation 85 will be taken to represent the voltage output of the $(m, n)^{th}$ detector including the chopper irradiance.

The action of the chopper in this model is assumed to be uniform translation in the positive x -direction, hence $V_y=0$. In addition, the chopper width is assumed to be an integral number of detector lengths, i.e., $\bar{j}\Delta x, \bar{j} =$

AD-A153 156

ANALYSIS AND MODELING FOR THERMAL FOCAL PLANE ARRAYS
(U) NICHOLS RESEARCH CORP ANN ARBOR MI T W TIER ET AL.
10 JUL 84 NRCA-TR-84-001 DAAK70-83-C-0026

272

UNCLASSIFIED

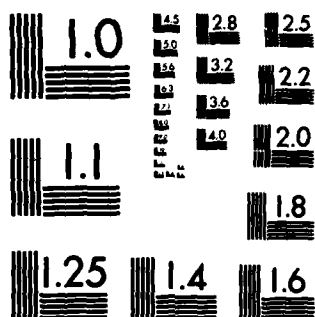
F/G 14/2

NL

END

FILMED

DTIC



MICROCOPY RESOLUTION TEST CHART
NATIONAL BUREAU OF STANDARDS-1963-A

integer >0 , and its length is essentially infinite (in the y -direction). A representation of this chopper is

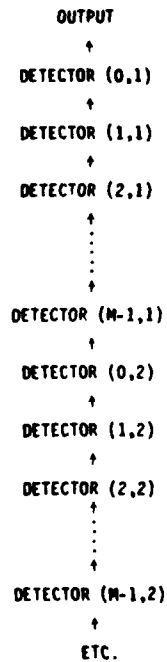
$$C(x_m - \xi - v_x t, y_m - \eta) = 1 + 2 \sum_{\lambda=1}^{\infty} \frac{2}{\pi \lambda} \sin\left(\frac{\pi \lambda}{2}\right) \cos\left[k_o \lambda \left(x_m - \xi - \frac{j \Delta x}{2} - v_x t\right)\right] \quad (87)$$

where

$$k_o \equiv \frac{2\pi}{\Delta x} \quad (88)$$

At $t=0$, the first j rows of detectors are covered by this chopper.

A somewhat simplified readout process is included in the model. Readout is represented as a sampling, in time, of the voltage output of Equation 85 with samples being read out sequentially in the order



for a total of $M \times N$ discrete spatial samples of the entire array in one frame time.

To establish notation, and to be more precise about the spatial and temporal sampling, write the output from one (arbitrary) point (x,y) in the focal plane, taken at time t , as

$$V(x,y;t) = \begin{cases} \tilde{V}(x,y,t) & 0 \leq x \leq (M-1)\Delta x \\ & 1 \leq y \leq N\Delta y \\ 0 & \text{Otherwise} \end{cases} \quad (89)$$

V given here by Equation 85 with (x,y) replacing (x_m,y_m) . Upon sampling, spatially, the voltage output will become a doubly periodic sequence, i.e., periodic in x with period M and periodic in y with period N . This spatial output can be represented as one period in M and one period in N of the sequence

$$\tilde{V}(x,y;t) = \sum_{k=-\infty}^{\infty} \sum_{l=-\infty}^{\infty} V(x+kM, y+lN; t). \quad (90)$$

where V is given by Equation 86. This V has the proper spatial behavior and represents the focal plane output which is sampled spatially and temporally (see, for example, Reference 14).

Spatial sampling is accomplished by taking $2J$ spatial samples over one detector length, Δx , at one detector sample per frame time. The sample time interval is derived from the sampling theorem for band-limited functions. That is, if all temporally varying inputs are band-limited to a band of width $2/T \text{ sec}^{-1}$, optimal sampling is at $T/2$ second time intervals. With a scan velocity V_x over the smallest length scale, $\Delta x/J$, $T = \Delta x/JV_x$. Spatial sampling in the direction of chopper motion is handled similarly. Without loss of generality, we assume spatial frequencies no greater than $J/\Delta x$ are present in the scene, hence sampling is done in intervals of length $\Delta x/2J$. Sampling in y results simply from indexing the temporal samples so as to obtain correspondence between the readout times and the detectors' y -coordinates (see below).

At this stage of our detector array modeling, steady-state response has been the focus of our analysis. Hence, in Equation 85, the system's temporal response will be assumed from here on to be instantaneous. In this case, the dt integration becomes trivial, reducing Equation 85 to the form

$$V(x,y;t) = \iint dx_1 dy_1 H(x-x_1, y-y_1) C(x-x_1-V_x t) I(x_1, y_1) \quad (91)$$

$$\equiv H(x,y) C(x-V_x t) ** I$$

where $**$ is used to signify a two-dimensional convolution. At this time, we will apply the sampling function which yields the CCD readout protocol described above. This sampling function incorporates the two characteristic clock cycles inherent in our readout procedure. The fastest of these clocks is the CCD device clock which runs at a rate such that an entire array is read out in a frame time, $\tau_s = \Delta x / 2J V_x$. For our $M \times N$ array, this clock has a period of τ_s / MN seconds and in the sampling function, the summation index j is associated with this clock period. Thus, to accomplish array readout in a frame time, a single detector voltage is output each CCD clock cycle beginning with the $(x = 0 \cdot \Delta x, y = \Delta y)$ spatial location, i.e., the upper left hand detector in Figure 1 alone. During the next CCD clock cycle, detector $(x = \Delta x, y = \Delta y)$ is readout, etc. After M CCD clock cycles, the y -coordinate is incremented and the x -coordinate is reset. After MN CCD clock ticks, one frame time, t is incremented one frame time, and the chopper's spatial location is incremented by $\Delta x / 2J$ (the chopper blade moves in the x -direction only). The x and y coordinates are reset and the readout procedure begins for the next frame. With V of Equation 91 obeying Equation 89 above, the spatially and temporally sampled, spatially periodic array output voltage at time t can be expressed in the form

$$V(x,y,t) = \sum_{j=-\infty}^{\infty} H(x,y) C(x-V_x t) ** I \delta \left\{ x - \left[\frac{\left(\frac{1}{MN} \right)^{\sim} \bmod(2J)}{2J} + j \bmod(M) \right] \Delta x \right\}$$

$$\cdot \delta \left[y - \left(\frac{1}{M} \right)^{\sim} \bmod(N) \Delta y \right] \cdot \delta \left(t - \tau_s \left[\frac{1}{MN} \right]^{\sim} \right) \quad (92)$$

where (a)' means take the integer part of a and $\delta\{\}$ is the usual delta function. Rewriting Equation 92 in a more convenient form by regrouping terms, the "integer part" notation can be incorporated to yield

$$\begin{aligned}
 V(x,y,t) = & \sum_{k=-\infty}^{\infty} \sum_{j=-(M-1)}^{M-1} \sum_{l=-(N-1)}^{N-1} H(x,y) C(x-v_x t) ** I \\
 & \cdot \delta \left\{ x - \left[\frac{k \bmod(2J)}{2J} + (j+lM+kNM) \bmod(M) \right] \Delta x \right\} \\
 & \cdot \delta \{ y - (l+kN) \bmod(N) \Delta y \} \delta \{ t + k \tau_s \} \quad (93)
 \end{aligned}$$

where the general result

$$\sum_{j=-\infty}^{\infty} A \left[j, \left(\frac{1}{M} \right)', \left(\frac{1}{NM} \right)' \right] = \sum_{k=-\infty}^{\infty} \sum_{j=-(M-1)}^{M-1} \sum_{l=-(N-1)}^{N-1} A(j+lM+kNM, l+kN, k) \quad (94)$$

has been used. The sequence of terms in Equation 93 whose indices are expressed modulo an integer can be treated as a single period of an infinite periodic sequence. For example, consider the $k \bmod(2J)$ index in the first delta function in Equation 93. Representing a general term in the summation over k as $Z[k \bmod(2J)]$ where, without loss of generality, all other k dependence may be temporarily neglected. For $0 \leq k \leq 2J-1$, the index $k \bmod 2J$ is simply k , and is zero for k outside this interval. Thus in this index, $k \bmod(2J)$, $Z[k \bmod(2J)]$ is a sequence of length $2J$. This sequence can be considered, alternatively, as a single period, of duration $2J$, of an infinite periodic sequence $\tilde{Z}[k]$ where

$$\tilde{Z}[k] = \sum_{r=-\infty}^{\infty} Z[k+2rJ] \quad (95)$$

Applying this to the indices $k \text{ Mod}(2J)$, $(j+lM+kMN) \text{ Mod}(M)$ and $(l+kN) \text{ Mod}(N)$ of Equation 93, the following expression results where summation indices have been combined when possible.

$$\begin{aligned} \tilde{V}(x,y,t) = & \sum_{k=-\infty}^{\infty} \sum_{j=-(M-1)}^{M-1} \sum_{l=-(N-1)}^{N-1} \sum_{\alpha=-\infty}^{\infty} \sum_{p=-\infty}^{\infty} H(x,y) C(x-V_x t) ** 1 \\ & \cdot \delta \left\{ x - \left(\frac{k}{2J} + \alpha + pN \right) \Delta x \right\} \\ & \cdot \delta \{ y - (l+kM)\Delta y \} \\ & \cdot \delta \{ t - [j+lM+kNM]\tau_s \} \quad (96) \end{aligned}$$

Prior to Fourier transforming in space and time, introduce the following expression for the three delta distributions in the last expression:

$$\delta(x) = \frac{1}{2\pi} \int_{-\infty}^{\infty} e^{ixy} dy \quad (97)$$

Interchanging the order of integration and summation, Equation 96 then takes the form:

$$\begin{aligned} \tilde{V}(x,y,t) = & \sum_{j=-(M-1)}^{M-1} \sum_{l=-(N-1)}^{N-1} H(x,y) C(x-V_x t) ** 1 \frac{1}{(2\pi)^3} \\ & \cdot \iiint_{-\infty}^{\infty} dS_1 dS_2 dS_3 e^{ixS_1} e^{i(y-l\Delta y)S_2} e^{itS_3} \\ & \cdot e^{-iS_3 lM\tau_s} e^{-iS_3 j\tau_s} \end{aligned}$$

$$\begin{aligned}
& \cdot \sum_{k=-\infty}^{\infty} e^{-ik \left(\frac{S_1 \Delta x}{2J} + S_1 M \Delta x + M N S_3 \tau_s \right)} \\
& \cdot \sum_{\alpha=-\infty}^{\infty} e^{-i\alpha(S_1 \Delta x)} \\
& \cdot \sum_{p=-\infty}^{\infty} e^{-ip(S_2 N \Delta y)} \quad (98)
\end{aligned}$$

The summations can be performed using the result

$$\sum_{n=-\infty}^{\infty} e^{ing} = 2\pi \sum_{n=-\infty}^{\infty} \delta(g - 2\pi n) \quad (99)$$

to yield

$$\begin{aligned}
\tilde{V}(x, y, t) = & 2\pi \sum_{j=-(M-1)}^{M-1} \sum_{\ell=-(N-1)}^{N-1} H(x, y) C(x - V_x t) \iint\limits_{-\infty}^{\infty} dS_1 dS_2 dS_3 \\
& \cdot e^{ixS_1} e^{iyS_2} e^{itS_3} e^{-iS_3(j+\ell M)\tau_s} e^{-i\ell\Delta y S_2} \\
& \cdot \sum_{\alpha, \beta, \delta=-\infty}^{\infty} \delta \left(\frac{S_1 \Delta x}{2J} + S_1 M \Delta x + M N S_3 \tau_s - 2\pi\alpha \right) \delta(S_1 \Delta x - 2\pi\beta) \\
& \cdot \delta(S_2 N \Delta y - 2\pi\delta) \quad (100)
\end{aligned}$$

Fourier transforming this last expression in (x,y,t) yields, upon interchanging the order of integration,

$$\begin{aligned}
 \hat{V}(k_x, k_y, \omega) = & 2\pi \sum_{j=-(M-1)}^{M-1} \sum_{l=-(N-1)}^{N-1} \int_{-\infty}^{\infty} \int_{-\infty}^{\infty} \int_{-\infty}^{\infty} dS_1 dS_2 dS_3 \sum_{\alpha, \beta, \delta=-\infty}^{\infty} \\
 & \cdot \delta \left(\frac{S_1 \Delta x}{2J} + S_1 M \Delta x + M N S_3 \tau_s - 2\pi \alpha \right) \delta(S_1 \Delta x - 2\pi \beta) \\
 & \cdot \delta(S_2 N \Delta y - 2\pi \delta) e^{-iS_3(j+lM)\tau_s} e^{-iS_2 l \Delta y} \\
 & \cdot \hat{H}(\Omega_x, \Omega_y) \hat{C}(\Omega_z) \hat{I}(\Omega_x + \Omega_z, \Omega_y)
 \end{aligned} \tag{101}$$

where:

$$\hat{H}(\Omega_x, \Omega_y) = \int_{-\infty}^{\infty} \int_{-\infty}^{\infty} dx dy e^{-ix\Omega_x} e^{-iy\Omega_y} H(x, y) \tag{102}$$

$$\hat{C}(\Omega_z) = \int_{-\infty}^{\infty} dz e^{-iz\Omega_z} C(z) \tag{103}$$

$$\hat{I}(\Omega_x + \Omega_z, \Omega_y) = \int_{-\infty}^{\infty} \int_{-\infty}^{\infty} dx dy e^{-ix(\Omega_x + \Omega_z)} e^{-iy\Omega_y} I(x, y) \tag{104}$$

where H is the array system transfer function including the geometry (i.e., spatial extent of array, detector length, width), C is the chopper and I is the input irradiance. The Ω 's (spatial frequencies) are defined as

$$\Omega_x = k_x - s_1 - \left(\frac{w-s_3}{v_x} \right) \quad (105)$$

$$\Omega_y = k_y - s_2 \quad (106)$$

$$\Omega_z = \frac{w-s_3}{v_x} \quad (107)$$

k_x and k_y are the spatial frequencies of the input irradiance and w is the output electrical frequency. Performing integrations in Equation 101,

$$\begin{aligned} \hat{V}(k_x, k_y, w) = & \frac{2\pi}{\tau_s N^2 M \Delta x \Delta y} \sum_{\alpha=-\infty}^{\infty} \sum_{\beta=-\infty}^{\infty} \sum_{\delta=-\infty}^{\infty} \sum_{j=-(M-1)}^{M-1} \sum_{\ell=-(N-1)}^{N-1} \\ & e^{-j \frac{2\pi \ell \delta}{N}} e^{-j 2\pi \left[\alpha - \beta \left(\frac{1}{2J} + M \right) \right] \frac{(j+\ell M)}{MN}} \\ & \hat{H}(\Omega_x, \Omega_y) \hat{C}(\Omega_z) \hat{I}(\Omega_x + \Omega_z, \Omega_y) \end{aligned} \quad (108)$$

where

$$\Omega_x = k_x - k_{ox} \beta - \frac{1}{v_x} \left[w - w_s \alpha + \beta w_s \left(\frac{1}{2J} + M \right) \right] \quad (109)$$

$$\Omega_y = k_y - k_{oy} \frac{\delta}{N} \quad (110)$$

$$\Omega_z = \frac{1}{v_x} \left[w - w_s \alpha + \beta w_s \left(\frac{1}{2J} + M \right) \right] \quad (111)$$

$$w_s \equiv \frac{2}{MN\tau_s}, \quad k_{ox} = \frac{2\pi}{\Delta x}, \quad k_{oy} = \frac{2\pi}{\Delta y} \quad (112)$$

The summations over j and l can be done to yield

$$\begin{aligned} \hat{V}(k_x, k_y, w) = & \frac{2\pi}{\Delta x \Delta y M N^2 \tau_s} \sum_{\alpha=-\infty}^{\infty} \sum_{\beta=-\infty}^{\infty} \sum_{\delta=-\infty}^{\infty} \hat{H}(\Omega_x, \Omega_y) \hat{C}(\Omega_z) \hat{I}(\Omega_x + \Omega_z, \Omega_y) \\ & \cdot \frac{\sin \left\{ \frac{2\pi}{MN} (M - \frac{1}{2}) \left[\alpha - \beta \left(\frac{1}{2J} + M \right) \right] \right\}}{\sin \left\{ \frac{\pi}{MN} \left[\alpha - \beta \left(\frac{1}{2J} + M \right) \right] \right\}} \\ & \cdot \frac{\sin \left\{ \frac{2\pi}{N} (N - \frac{1}{2}) \left[\alpha + \delta - \beta \left(\frac{1}{2J} + M \right) \right] \right\}}{\sin \left\{ \frac{\pi}{N} \left[\alpha + \delta - \beta \left(\frac{1}{2J} + M \right) \right] \right\}} \end{aligned} \quad (113)$$

for the Fourier transform of the array output voltage as a function of spatial and electrical frequencies. Note that Ω_x , Ω_y and Ω_z are functions of α , β and δ (see Equations 109 through 111). This expression contains the general relationship of input spatial frequencies, k_x and k_y , to the output electrical frequency, w . This can be brought out by inserting the Fourier transform of the chopping function, the system transfer function and an irradiance distribution. Using Equation 88 above, the transform, $\hat{C}(\Omega_z)$, is:

$$\hat{C}(\Omega_z) = \pi \delta(\Omega_z) + 2 \sum_{\lambda=1}^{\infty} \frac{1}{\lambda} \sin\left(\frac{\pi\lambda}{2}\right) \left\{ e^{-i\lambda k_c \bar{j} \frac{\Delta x}{2}} \delta(\Omega_z - k_c \lambda) + e^{i\lambda k_c \bar{j} \frac{\Delta x}{2}} \delta(\Omega_z + k_c \lambda) \right\} \quad (114)$$

where

$$k_c = \frac{2\pi}{j\Delta x} \quad (115)$$

For a system transfer function, assume a simple $M \times N$ rectangular array (as in Figure 85 above). The Fourier transform of the system function is (up to a phase)

$$\hat{H}(\Omega_x, \Omega_y) = e^{i\phi(M,N)} e^{-i \frac{\Delta x}{2} \Omega_x \frac{\sin \left(M \frac{\Delta x}{2} \Omega_x \right)}{\left(\frac{\Omega_x}{2} \right)}} e^{-i \frac{\Delta y}{2} \Omega_y \frac{\sin \left(N \frac{\Delta y}{2} \Omega_y \right)}{\left(\frac{\Omega_y}{2} \right)}} \quad (116)$$

where $\phi(M,N)$ is an inessential phase dependent only on M and N . To specify an irradiance, $I(x,y)$ is taken to be a line source of infinite extent in the y -direction lying across the p^{th} row of detectors at an x -coordinate of $(p + q/2J) \Delta x$, i.e.,

$$I(x,y) = \frac{I_0}{N} \delta \left[x - \left(p + \frac{q}{2J} \right) \Delta x \right], \quad \begin{array}{l} p = 0, 1, \dots, M-1 \\ q = 1, 2, \dots, 2J \end{array} \quad (117)$$

hence its Fourier transform is

$$\hat{I}(\Omega_x + \Omega_z, \Omega_y) = 2\pi \frac{I_0}{N} e^{-i \left(p + \frac{q}{2J} \right) \Delta x (\Omega_x + \Omega_z)} \delta(\Omega_y) \quad (118)$$

$I(x,y)$ has been normalized such that summing over a row of detectors in the y -direction yields the total irradiance input to the array. Instead of using these transforms in the general expression (Equation 113), Equation 109, written in a slightly different form, will be used. To simplify, Equation 109 for the example being considered, using the delta function in Ω_y which appears in the example irradiance (see Equation 118 above), the sum over δ can be given the form

$$\sum_{\delta=-\infty}^{\infty} e^{-2\pi i \ell \frac{\delta}{N}} \delta(\Omega_y) \rightarrow \sum_{\gamma=-\infty}^{\infty} e^{-i \ell k_y \Delta y} \delta \left(k_y - \gamma \frac{k_{oy}}{N} \right) \quad (119)$$

where the summation index, δ , has been replaced by γ . In addition, the Fourier transform of the system function $\hat{H}(\Omega_x, \Omega_y)$ can be simplified to

$$\hat{H}(\Omega_x, 0) = N \Delta y e^{i\phi(M, N)} e^{-i \frac{\Delta x}{2} \Omega_x} \frac{\sin \left(M \frac{\Delta x}{2} \Omega_x \right)}{\left(\frac{\Omega_x}{2} \right)} \quad (120)$$

by utilizing the $\Omega_y=0$ condition from Equation 118. Further simplification can be obtained by noting the summation index α appears only in the combination $\alpha - \beta M$ with the index β (see Equations 110 and 112). Hence shifting the summation in α , Equations 110 through 112 become

$$\Omega_x = k_x - \beta k_{ox} - \frac{1}{V_x} \left\{ w - \left(\alpha - \frac{\beta}{2J} \right) w_s \right\} \quad (121)$$

$$\Omega_y = k_y - \frac{\delta}{N} k_{oy} \quad (122)$$

$$\Omega_z = \frac{1}{V_x} \left\{ w - \left(\alpha - \frac{\beta}{2J} \right) w_s \right\} \quad (123)$$

The summation in β also can be shifted, i.e.,

$$\beta \leftarrow 2J\alpha - \beta \quad (124)$$

With this change,

$$\Omega_x = k_x - 2J\alpha k_{ox} + \beta k_{ox} - \frac{1}{V_x} \left(w - \frac{\beta}{2J} w_s \right) \quad (125)$$

and

$$\Omega_z = \frac{1}{V_x} \left(w - \frac{\beta}{2J} w_s \right) \quad (126)$$

Using these simplifications, Equation 107 is now of the form

$$\begin{aligned}
 \hat{V}(k_x, k_y, w) = & \frac{2\pi \cdot 2\pi I_o}{MN^2 \tau_s \Delta x} e^{i\phi(M,N)} \sum_{\alpha=-\infty}^{\infty} \sum_{\beta=-\infty}^{\infty} \sum_{\gamma=-\infty}^{\infty} \sum_{j=-(M-1)}^{M-1} \sum_{\ell=-(N-1)}^{N-1} \\
 & \cdot e^{-2\pi i \frac{\beta}{2J} (j+\ell M) \frac{1}{MN}} \cdot \hat{C}(\Omega_z) \\
 & \cdot \left\{ e^{-i \frac{\Delta x}{2} \Omega_x} e^{-i \left(p + \frac{q}{2J}\right) (\Omega_x + \Omega_z) \Delta x} \frac{\sin\left(M \frac{\Delta x}{2} \Omega_x\right)}{\left(\frac{\Omega_x}{2}\right)} \right\} \\
 & \cdot e^{-i \ell k_y \Delta y} \delta \left\{ k_y - \gamma \frac{k_{oy}}{N} \right\} \quad (127)
 \end{aligned}$$

Since only the bracketed terms in this last equation are dependent upon α , the summation over α can be performed. Focusing on the bracketed terms only, the summation in α is of the form

$$\sum_{\alpha} \{ \} = M \Delta x e^{-i \left\{ \frac{w}{2} + \left(p + \frac{q}{2J}\right) (k_x + \beta k_{ox}) \right\} \Delta x} \sum_{\alpha=-\infty}^{\infty} e^{i\alpha A} f(z - \alpha B) \quad (128)$$

where: $A \equiv 2\pi J \left\{ 1 + 2 \left(p + \frac{q}{2J}\right) \right\}$

$B \equiv 2\pi J M$

$Z \equiv M \frac{\Delta x}{2} w_x$

$w_x \equiv k_x + \beta k_{ox} - \frac{1}{v_x} \left\{ w - \frac{\beta w_s}{2J} \right\}$

$f(x) = \frac{\sin x}{x}$

Using Poisson's summation formula, the sum in Equation 128 can be carried out to yield

$$\sum_{\alpha=-\infty}^{\infty} e^{i\alpha A} f(z-\alpha B) = \frac{2\pi}{B} \sum_{\alpha=-\infty}^{\infty} F\left(\frac{2\pi\alpha+A}{B}\right) e^{i\frac{z}{B}(2\pi\alpha+A)} \quad (129)$$

with

$$F(x) = \int_{-\infty}^{\infty} f(y) e^{ixy} dy \quad (130)$$

$$= \begin{cases} \pi & -1 < x < 1 \\ 0 & \text{Otherwise} \end{cases} \quad (131)$$

Using the restriction in Equation 130, Equation 129 becomes

$$\sum_{\alpha=-\infty}^{\infty} e^{i\alpha A} f(z-\alpha B) = \frac{2\pi}{B} \sum_{\alpha=\alpha_-}^{\alpha_+} e^{i\frac{z}{B}(2\pi\alpha+A)} \quad (132)$$

where α_{\pm} satisfies

$$\left| \alpha_{\pm} + \frac{A}{2\pi} \right| < JM, \quad (133)$$

i.e.,

$$\alpha_+ \equiv JM - \frac{A}{2\pi} \quad (134)$$

$$\alpha_- \equiv -JM - \frac{A}{2\pi} \quad (135)$$

With these results, Equation 128 becomes

$$\sum_{\alpha} \{ \} = \frac{\pi \Delta x}{J} e^{-1 \frac{\Delta x}{V_x} \left(p + \frac{q}{2J} \right) \left(w - \frac{\beta w_s}{2J} \right)} \sum_{\alpha=\alpha_-}^{\alpha_+} e^{1 \frac{w_x \Delta x}{2J} \alpha} \quad (136)$$

Before using this in Equation 127, it is convenient to note an alternative form for $\hat{C}(\Omega_z)$ appearing in that equation. $\hat{C}(\Omega_z)$, given in Equation 114 above, can be written as

$$\hat{C}(\Omega_z) = 2 \sum_{\lambda=-\infty}^{\infty} \frac{1}{\lambda} \sin\left(\frac{\pi \lambda}{2}\right) e^{-i \lambda k_c \bar{j} \frac{\Delta x}{2}} \delta(\Omega_z - k_c \lambda) \quad (137)$$

Using this form for $\hat{C}(\Omega_z)$ and the results from Equation 136, Equation 127 becomes

$$\begin{aligned} \hat{V}(k_x, k_y, w) &= \frac{8\pi^3 I_o V_x}{JMN^2 \tau_s} e^{i\phi(M,N)} \\ &\cdot \sum_{\alpha=\alpha_-}^{\alpha_+} \sum_{\gamma=-\infty}^{\infty} \sum_{\lambda=-\infty}^{\infty} \sum_{j=-(M-1)}^{M-1} \sum_{l=-(N-1)}^{N-1} \sum_{\beta=-\infty}^{\infty} \\ &\cdot e^{i \frac{\pi}{J} \left\{ \alpha - \left(\frac{j+lM}{MN} \right) \right\} \beta} \delta \left\{ w - V_x k_c \lambda - \frac{\beta w_s}{2J} \right\} \\ &\cdot \frac{(-1)^\lambda}{\lambda} \sin\left(\frac{\pi \lambda}{2}\right) e^{-i k_c \Delta x \left(p + \frac{q}{2J} \right) \lambda} e^{i \frac{\Delta x}{2J} (k_x - k_c \lambda) \alpha} \\ &\cdot e^{-i l k_y \Delta y} \delta \left\{ k_y - \frac{\gamma k_{oy}}{N} \right\} \quad (138) \end{aligned}$$

Using the limits α_{\pm} from Equations 134 and 135, the summation in α can be carried out yielding

$$\sum_{\alpha=\alpha_-}^{\alpha_+} e^{iG\alpha} = e^{-i \frac{AG}{2\pi}} \frac{\sin \{(JM+\frac{1}{2})G\}}{\sin \{G/2\}} \quad (139)$$

where

$$G \equiv \frac{\pi\beta}{J} + \frac{\Delta x}{2J} (k_x - k_c \lambda) \quad (140)$$

and A is defined in Equation 128. For M large, the limit as $M \rightarrow \infty$ of Equation 139 provides a reasonable approximation to sampled array behavior. Taking this limit, the α summation becomes

$$e^{-i \frac{AG}{2\pi}} \frac{\sin \{(JM+\frac{1}{2})G\}}{\sin \{G/2\}} \xrightarrow{M \rightarrow \infty} 2\pi \delta(G) \quad (141)$$

Equation 138 now becomes

$$\begin{aligned} \hat{V}(k_x, k_y, w) = & 8\pi^2 \frac{I_o}{N} k_{ox} w_s e^{i\phi(M,N)} \\ & \cdot \sum_{\beta=-\infty}^{\infty} \sum_{\gamma=-\infty}^{\infty} \sum_{\lambda=-\infty}^{\infty} \sum_{j=-(M-1)}^{M-1} \sum_{l=-(N-1)}^{N-1} \\ & \cdot e^{-i \frac{\pi}{J} \left(\frac{j+lM}{MN} \right) \beta} \frac{(-1)^\lambda}{\lambda} \sin\left(\frac{\pi\lambda}{2}\right) e^{-ik_c \Delta x \left(p + \frac{q}{2J} \right) \lambda} \\ & \cdot e^{-i l k_y \Delta y} \delta\left(\frac{w}{v_x} - k_x - 2k_{ox}\beta\right) \delta(k_x + k_{ox}\beta - k_c \lambda) \delta\left(k_y - \frac{\gamma k_{oy}}{N}\right) \end{aligned} \quad (142)$$

For consistency, the large M,N limit should be taken in this last expression as done in the summation over α . In doing this, the sums over j and l diverge as $2N$ and $2M$, respectively. However, w_s behavior as $(MN)^{-1}$, thus together

$$w_s \sum_j \sum_l \frac{1}{M, N \rightarrow \infty} \rightarrow \frac{8\pi}{T_s} \quad (143)$$

Some care is required in taking the large N limit in the summation over the k_y delta function. This limit is

$$\lim_{N \rightarrow \infty} \frac{1}{N} \sum_{\gamma=-\infty}^{\infty} \delta \left(k_y - \frac{\gamma k_{oy}}{N} \right) = \frac{1}{k_{oy}} \quad (144)$$

This result follows by first applying the sampling distribution of Equation 144 to test functions $\phi(x)$ which, without loss of generality, are taken to be normalized, i.e.,

$$\int_{-\infty}^{\infty} \phi(x) dx = 1 \quad (145)$$

Replacing the δ distributions with the representation,

$$\delta(z) = \lim_{t \rightarrow \infty} \frac{\sin(zt)}{\pi z} \quad (146)$$

the sampling represented by Equation 144 takes the form

$$\frac{1}{\pi k_{oy}} \lim_{N \rightarrow \infty} \frac{1}{N} \sum_{\gamma=-\infty}^{\infty} \lim_{t \rightarrow \infty} \int_{-\infty}^{\infty} \phi(x) \frac{\sin \left\{ t \left(x - \frac{\gamma}{N} \right) \right\}}{\left(x - \frac{\gamma}{N} \right)} dx \quad (147)$$

where k_{oy} has been pulled out of the δ distribution using the relation

$$\delta(ax) = \frac{1}{|a|} \delta(x) \quad (148)$$

so $x \equiv k_y/k_{oy}$ is dimensionless. Changing variables, Equation 147 becomes

$$\frac{1}{\pi k_{oy}} \lim_{N \rightarrow \infty} \frac{1}{N} \sum_{\gamma=-\infty}^{\infty} \lim_{t \rightarrow \infty} \left(\int_{-\infty}^{-\Delta} + \int_{\Delta}^{\infty} + \int_{-\Delta}^{\Delta} \right) \phi \left(x + \frac{\gamma}{N} \right) \frac{\sin(tx)}{x} dx \quad (149)$$

where the integral has been written as a sum of three terms. Since $\phi(x + \gamma/N)x^{-1}$ is integrable over the $(-\infty, -\Delta)$ and (Δ, ∞) intervals, it follows from the Riemann-Lebesgue lemma that the first two terms of Equation 149 tend to zero as $t \rightarrow \infty$. For Δ sufficiently small, $\phi(x + \gamma/N) \approx \phi(\gamma/N)$ since ϕ is continuous. With this Equation 149 becomes

$$\frac{1}{\pi k_{oy}} \lim_{N \rightarrow \infty} \frac{1}{N} \sum_{\gamma=-\infty}^{\infty} \lim_{t \rightarrow \infty} \phi \left(\frac{\gamma}{N} \right) \int_{-\Delta}^{\Delta} \frac{\sin(tx)}{x} dx \quad (150)$$

With a change of variables, $xt=n$, and the result

$$\int_{-\infty}^{\infty} \frac{\sin(x)}{\pi x} dx = 1 \quad (151)$$

Equation 150 takes the form

$$\frac{1}{k_{oy}} \lim_{N \rightarrow \infty} \sum_{\gamma=-\infty}^{\infty} \frac{1}{N} \phi \left(\frac{\gamma}{N} \right) \quad (152)$$

For large N , the summation can be replaced by a Riemann integral with the identifications

$$\frac{Y}{N} \rightarrow x, \quad \frac{1}{N} \rightarrow dx \quad (153)$$

to yield

$$\frac{1}{k_{oy}} \lim_{N \rightarrow \infty} \int_{-\infty}^{\infty} \phi(x) dx, \quad (154)$$

which is independent of N , hence the limit becomes trivial. Since the test functions were taken to be normalized, the result on the right hand side of Equation 144 follows. Combining this and the result in Equation 143, the voltage output of Equation 142 becomes

$$V(k_x, k_y, w) = \frac{64\pi^3 I_o k_{ox}}{\tau_s k_{oy}} \sum_{\beta=-\infty}^{\infty} \sum_{\lambda=-\infty}^{\infty} \frac{1}{\lambda} \sin\left(\frac{\pi\lambda}{2}\right) e^{-j\{k_c \Delta x (p + \frac{q}{2J}) + \pi\}\lambda} \\ \cdot \delta\left(\frac{w}{v_x} - k_x - 2k_{ox}\beta\right) \delta(k_x + k_{ox}\beta - k_c\lambda) \quad (155)$$

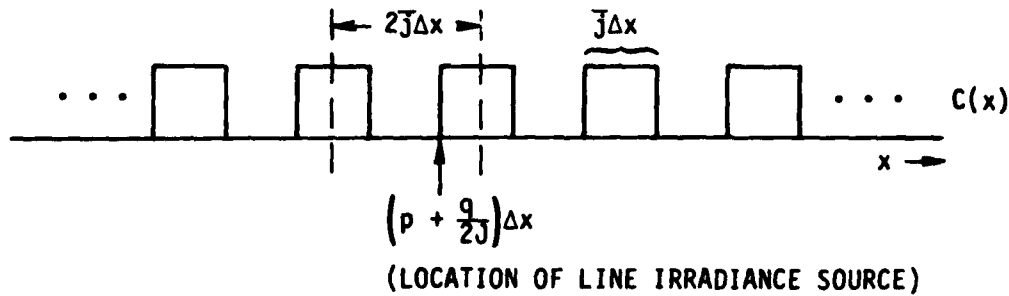
The summation over λ in this result is simply the Fourier transform (in the frequency variable $k_x + k_{ox}\beta$) of the square pulse sequence depicted in Figure 19a. The exponential is a phase shift reflecting the chopper initial position and it has no effect on the amplitude spectrum. These pulses are of width $j\Delta x$, i.e., the physical chopper blade covers j detector elements each of length Δx in the x -direction, the direction of chopper motion.

The spacing between pulses is $2j\Delta x$, so the chopper has, in this model, a 50 percent duty cycle. At $t=0$, the edge of a blade is aligned with the line source of irradiance at the x coordinate $(p + q/2j)\Delta x$. The chopper and line source are, as mentioned earlier, assumed to be of infinite extent in the y -direction (out of the page in Figure 19). The Fourier transform of this pulse train, which appears in Equation 155, is shown in Figure 19b for β equal to a fixed integer. The transform is a line spectrum [entered at multiples of $k_{0x} \equiv 2\pi/\Delta x$, each line of which has side bands of decreasing amplitude at multiples of $k_c = 2\pi/j\Delta x$].

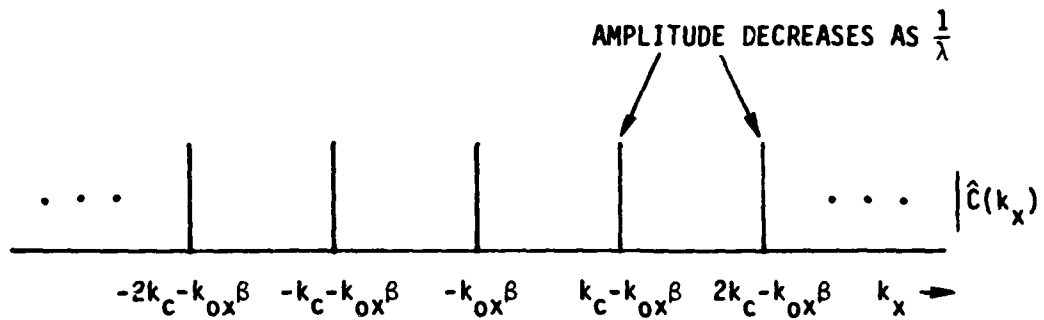
In Figure 19c, the voltage amplitude spectrum is plotted, at fixed β , as a function of normalized electrical frequency w/V_x whose units are radians per length. The complete voltage amplitude spectrum, for the infinite array-chopped infinite line source approximation, would be a superposition of an infinite set of spectra like Figure 19c, each with a different integer value β . This superposed set of spectra, one for each integer value of β , is the result of the specialization of the general equation, Equation 113, to the case of a sampled, infinite two-dimensional array with a chopped line irradiance source.

In the case where the two-dimensional array is treated as finite, each of the pulses appearing in Figure 19c would appear as broad $|\sin Ax/x|$ pulses. This would in turn potentially cause serious aliasing difficulties. In an approach to minimizing such problems by a study of tradeoffs involving chopper characteristics as well as detector response characteristics, Equation 113 should prove to be extremely useful.

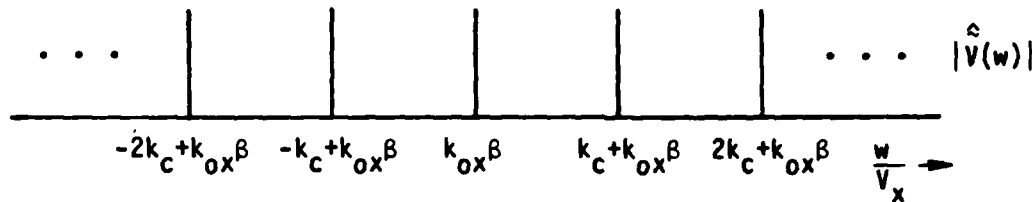
When fully integrated with the code developed during this contract, the general treatment given in this appendix (expressed in Equation 113) of a sampled two-dimensional rectangular array, with an arbitrary, chopped irradiance input, should provide a significant tool in simulation and design of pyroelectric arrays.



- (a) SCHEMATIC OF THE SPATIAL EXTENT (IN THE DIRECTION OF MOTION) OF THE CHOPPER; EACH BLADE IS \bar{J} DETECTOR ELEMENTS WIDE, AND SPACED $2\bar{J}$ ELEMENTS APART. INITIAL POSITION OF CHOPPER BLADE RELATIVE TO THE LINE SOURCE IS ALSO INDICATED.



- (b) SPECTRUM OF SAMPLED SPATIAL FREQUENCIES FOR β EQUAL TO FIXED INTEGER.



- (c) VOLTAGE AMPLITUDE SPECTRUM AS A FUNCTION OF NORMALIZED ELECTRICAL FREQUENCIES (NORMALIZED TO CHOPPER VELOCITY) FOR THE SAME VALUE OF β AS APPEARS IN THE SPATIAL FREQUENCY SPECTRUM OF (b) ABOVE.

FIGURE 19.

END

FILMED

5-85

DTIC